ABSTRACT

A STUDY OF THE F_3 LAYER AND IONOSPHERIC HORIZONTAL GRADIENT OBSERVED BY THE ARECIBO INCOHERENT SCATTER RADAR

by Zhengguang Wu

The electron density, line of sight velocity, and ion and electron temperatures of the ionosphere during Jul. 10 - 12, 2015 have been measured by the Arecibo Incoherent Scatter (ISR). This thesis focuses on three aspects. The first one is to study the F_3 layer, an additional layer above the traditional F_2 layer. The ionosphere F-region only has a single peak at about 300 km. This thesis reports the first observation and study of the F_3 layer phenomenon above Arecibo. The second aspect is to study the variations of the ionospheric horizontal gradients. The ionospheric horizontal gradients can be obtained from the gradient of the electron density and spatial difference of the peak altitude of the F_2 layer. We describe several methods for analyzing the changes of horizontal gradients. A detailed discussion on the ionospheric gradient direction is presented. The third aspect is to analyze the differences and relationships between electron temperature, ion temperatures and their ratio.

A STUDY OF THE F_3 LAYER AND IONOSPHERIC HORIZONTAL GRADIENT OBSERVED BY THE ARECIBO INCOHERENT SCATTER RADAR

A Thesis

Submitted to the

Faculty of Miami University

in partial fulfillment of

the requirements for the degree of

Master of Science in Computational Electrical and Computer Engineering
Department of Electrical and Computer Engineering

by

Zhengguang Wu

Miami University

Oxford, Ohio

2017

Advisor: Qihou Zhou

Reader: Dmitriy Garmatyuk

Reader: Yun Gong

This Thesis titled

A STUDY OF THE F_3 LAYER AND IONOSPHERIC HORIZONTAL GRADIENT OBSERVED BY THE ARECIBO INCOHERENT SCATTER RADAR

by

Zhengguang Wu

has been approved for publication by

College of Engineering and Computing

and

Department of Electrical and Computer Engineering

_____

Qihou Zhou

_____

Dmitriy Garmatyuk

_____

Yun Gong

Table of Contents

Contents

List of Tables

List of Figures

Chapter 1 Introduction

1.1 Introduction of the Incoherent Scatter Radar

Incoherent scatter radar is used to observe the phenomena occurring in the ionosphere. Power scattered from the ionosphere plasma by individual scatters makes up the overall scattering power of an incoherent scatter radar. Power returned from each altitude is proportional to electron density [Gong, 2012]. Some basic parameters, such as plasma line frequency, ion temperature, line of sight velocity can be acquired from incoherent scatter spectrum. After processing these basic information, we can further obtain additional useful information, such as maximum electron density (Nmf_2), maximum ionization height (Hmf_2) and vector velocities. Incoherent scatter radar is one of the most fundamental and important tools for us to study ionosphere.

1.1.1 History of Incoherent Scattering

Scattering power from free electrons in radar echoes has been ignored because of their extremely tiny power. In 1958, William E. Gordon first proposed an idea about a ground-based instrument for studying ionosphere [Gordon, 1958]. According to his theory, if a radar transmits a beam of wave to scatter electrons in ionosphere, it can return a tiny percentage of the power of the wave by free electrons. By processing the received incoherent scatter signal, information about electron density can be obtained. Later that year, Bowles verified Gordon's idea by an ISR experiment. He proved that the ISR has enough sensitivity to observe incoherent scatter power from free electrons [Bowels, 1958]. In 1969, J. V. Evans summarized ionosphere studies using measurements of electron density, electron temperature and ion temperature [Evans, 1969]. After that, incoherent scattering study of the ionosphere gradually matured and became one of the main methods to study ionosphere.

1.1.2 Radar Equation and Cross Section

Two of the most important aspects about an ISR are the radar equation and the cross section. The radar equation provides the relationship between the transmitted power and the received power. The following ISR equation is taken from the doctoral thesis of Yun Gong [Gong, 2012]. The incidental power on an electron is,

$$F_{\mathrm{i}}(\theta,\phi)=\frac{P_T L G(\theta,\phi)}{4\pi R^2} \tag{1.1}$$

where P_T represents the transmitted power and R is the range. $G(\theta, \phi)$ represents the antenna power gain, where θ and ϕ are the zenith and azimuth angle of the antenna in degrees, respectively. L represents the efficiency of the radar system. If the radar uses the same antenna to send and receive signal, power received by the radar is,

$$F_s(\theta,\phi)=\frac{F_i(\theta,\phi)\sigma(R,\omega)}{4\pi R^2} \tag{1.2}$$

$\sigma(R,\omega)$ represents the back scatter cross section. ω is the frequency. According to equation (1.1) and (1.2), we can derive the received power at range R, frequency ω when antenna works at θ degrees of zenith angle and ϕ degrees of azimuth angle,

$$P_s(\theta,\phi,R,\omega)=\frac{P_T L \lambda^2 G^2(\theta,\phi)\sigma(R,\omega)}{64\pi^3 R^4} \tag{1.3}$$

where λ represents the wavelength of the ISR. The premise of equation (1.3) is that the target of detection is a simple point.

The scattering cross section for an ISR can be shown to be.

$$\sigma=\sigma_e\cdot N=4\pi(r_e\sin(\phi))^2\cdot N \tag{1.4}$$

where σ_e represents cross section from a single electron. N, the total electron number. R_e, the radius of an electron [Evans, 1969].

1.1.3 Arecibo Incoherent Scatter Radar

In 1958, William E. Gordon conceived the idea of a 1000ft (305m) single-dish radio telescope at Arecibo, Puerto Rico after he refined the theory of incoherent scattering. Two years later, the construction of the Arecibo Ionospheric Observatory (AIO) started. It was funded by the US Department of APRA (Advanced Research Projects Agency) and evolved into one of the major bases for studies of the ionosphere in 1970s [Mathews, 2013]. At the present, it is used for

studies of the ionosphere and atmosphere, radio and planetary radar astronomy. Below is a top-view of the Arecibo ISR system:

Figure 1.1 A top-view of the Arecibo ISR system

http://www.astronomy.com/media/Images/News%20and%20Observing/News/2016/03/AreciboObservatory.jpg

The aperture diameter of the Arecibo ISR system is 305 meters. It is the largest single-dish ISR and the most sensitive and sophisticated incoherent scatter facility in use at present. The linear feed of Arecibo ISR is called the linefeed and it is 96 feet in length. Because of the spherical shape of the reflector, feeds can move as far as 20 degrees from zenith. The antenna aperture of Arecibo ISR is 41.7 dB/m^2 [Gong, 2012]. The ISR transmitter system operates at 430 MHz, which is very similar to the transmitter of the Millstone ISR (440Mhz). Litton L-5773 klystrons with 1 MHz bandwidth are used to make the nominal peak power of Arecibo ISR system attain 2.5 MW [Mathews, 2013]. In 1997, the Arecibo ISR system made an important upgrade. Another feed, a Gregorian system, was placed over the 305m dish. This upgrade allows dual beam ISR operations and makes the radar frequency range from about 3 MHz to 10 GHz [Sulzer et al., 1982 and Williams, 2015].

The high sensitivity of the Arecibo ISR makes it possible to observe the plasma lines for the study of electron parameters. In this thesis proposal, according to the ionospheric data recorded by Arecibo ISR in July, we found that electron density anomalously changed in the early morning of July 11. There was an additional layer above the typically observed F_2 layer. This additional layer is called F_3 layer. Then we use Arecibo ISR data of four days from July 10th to July 13th to analyze this abnormal phenomenon. A detailed data analysis is showed in the next chapter.

1.1.4 Incoherent Scatter Facilities

Several incoherent scatter facilities were built all over the world after 1960. Most of them are supported by the United States. Arecibo Observatory is the world's sensitive and arguably best known single-dish incoherent scatter radar. The newly built Arecibo-type telescope, FAST (Five hundred meter aperture spherical radio telescope), in Guizhou Province of southern China surpassed Arecibo and became the world's largest single aperture telescope with a aperture diameter of 500m. FAST, however, does not have a transmitter and is used only for radio astronomy. Table 1 lists the information of the most representative IS facilities in the world [Beynon and William 1978].

Table 1. Locations and parameters of the ISR stations

Facility	Location	Latitude / Longitude	Antenna	Operating Frequency	Peak Power
Jicamarca Radio Observatory	Lima, Peru	11.9° S / 76.9° W	Array of 18432 Dipole elements	49.9MHz	4MW
Millstone Hill Observatory	Westford U.S.	42.6° N / 71.5° W	68m parabola 25m parabola	440MHz 1295MHz	3MW 4MW

Chatanika ISR	Poket Flat Alaska U.S.	65° N 147° W	128 block like panels	430MHz-450MHz	2MW
The Sondrestrom Research Facilities	Sondrestrom Greenland	67° N 51° W	32m Fully steerable	1290MHz	3.5MW
Kharkov ISR	Kharkov Ukraine	48.5° N 36° E	100m parabola	150MHz	2MW
Arecibo Observatory	Arecibo, Puerto Rico	18.3° N 66.8° W	305m Spherical reflector	430MHz	2.5MW
FAST	Guizhou Province China	25.48° N 107.21° E	500m active reflector	70MHz-3GHz	N

1.1.5 Comparison with FAST

FAST, the Five hundred meter Aperture Spherical radio Telescope, is an Arecibo type spherical telescope. It was completed on July 3, 2011 and became the largest radio telescope in the world. These two giant single-dish radio telescopes are similar. They both use the natural “karst” hollows to fit the main reflectors. The static structures of two telescopes have resemblances.

While the platform of Arecibo telescopes hangs in a fixed place by three big pillars, the mobile range of the overhead receiver is limited by the space of overhanging platform. The overhead receiver of FAST is controlled by an ingenious robot based on six pulleys and six cables (see figure 1.2), which can make the receiver place on any position above the dish [Williams, 2015].

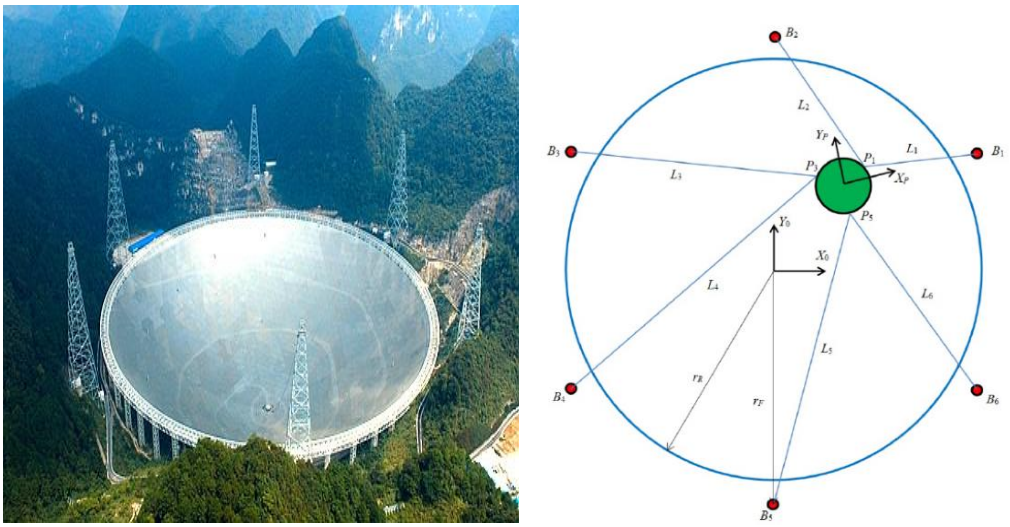

Figure 1.2 A top-view of the FAST and six active cables of FAST

http://www.icswb.com/upload/document_news/163/20160924/document_news_content_57e67d96d679f.jpg and [Williams, 2015]

The other main difference is that unlike the Arecibo telescope which uses a fixed spherical reflector with a diameter of 305 meters, FAST has an active reflector with a diameter of 500 meters. The active main reflector uses cable-net structure to change the spherical mirror and creates different parabolic shapes. This allows FAST make use almost all of its 500 meters dish while Arecibo telescope can only use 221 meters of its 305 meters dish [Nan, 2005].

1.2 Introduction of the Ionosphere

The ionosphere is the middle part between neutral atmosphere and the completely ionized atmosphere of the earth [Kelly, 1989]. It is a partially ionized gas, due to solar and cosmic radiation. It ranges from about 60 km to 1000 km and is composed of parts of the exosphere, mesosphere and thermosphere. During the daytime, sun and cosmic rays ionize the ionosphere. During the nighttime, only cosmic rays affect ionosphere. This makes ionosphere much less charged and many ionospheric phenomena are easier to recognize at night. The following parts are mainly about the structure of the neutral atmosphere and the ionosphere, daytime atmospheric composition, the main layers of the ionosphere and an introduction of an additional layer, i.e., the F_3 layer.

1.2.1 Structure of the Neutral Atmosphere and the Ionosphere

Under the influence of the earth's gravity, the ionosphere and atmosphere are horizontally stratified. The vertical structure of the ionosphere can be neatly illustrated by a representative plasma density profile and the vertical structure of atmosphere can be briefly illustrated by a typical temperature profile. Figure 1.3 shows a typical temperature profile of the atmosphere and a plasma density profile of ionosphere.

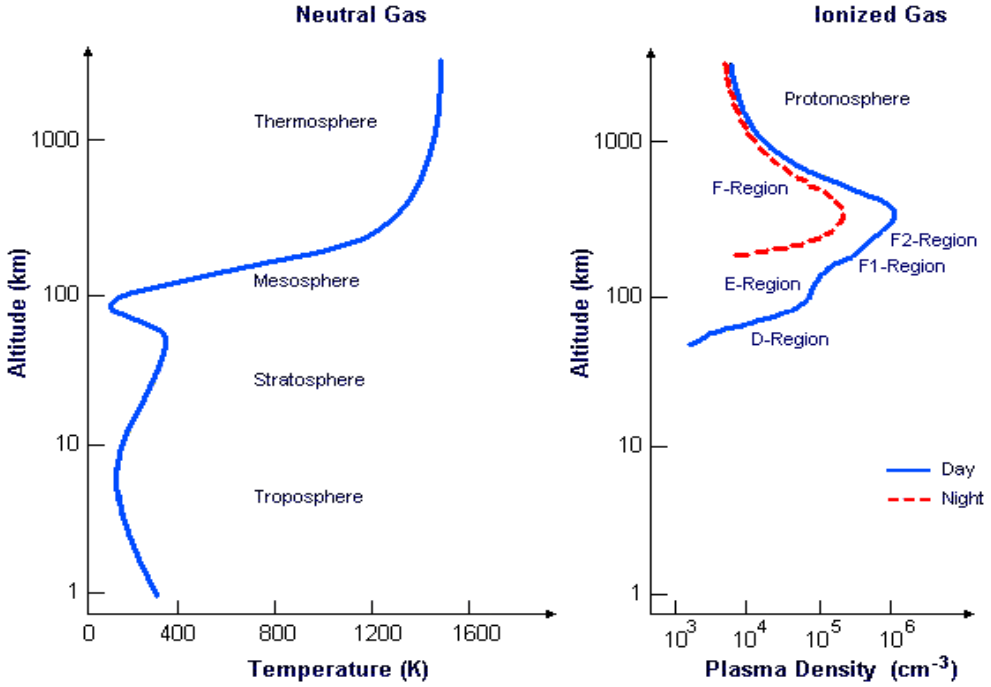

Figure 1.3 Temperature profile of atmosphere and plasma density profile of ionosphere
http://www.astrosurf.com/luxorion/Radio/atmosphere-ionosphere.gif

For the plasma density profile of ionosphere, there are two plasma density lines in the figure. The blue line represents the condition of ionosphere in daytime and red dashed line represents the ionosphere during nighttime. The peak of plasma density appears about 300 km which belongs to the F region and it can attain 10^6 cm^{-3} at noontime. The recombination rate (rate for electrons and ions combine to form neutral molecules and atoms) is the main limiting factor for the value of peak plasma density. Below 300 km, the plasma density of ionized gas falls exponentially with the decrease of altitude. For the nighttime profile, the plasma density below the F peak falls fast. The reason is that the lower altitude is dominated by the molecular ions, which are reduced radically in nighttime.

Turning to the temperature profile of the atmosphere on the left part of Figure 1.3, the temperature decreases with a rate of 7k/km from 1km to about 10km. Then it reverses and

increases with altitude until 50km. At about 80 km, there is an obvious bite-out form, where the temperature falls to about 170K at that point. This is related to radiative cooling effect [Kelly, 1989]. Above 100km, the temperature increases sharply and exceeds 1000K at about 200km, then it becomes stable.

1.2.2 Daytime Atmospheric Composition

Below 100 km, the dominant species of atmosphere are N_2 and O_2 which make up about 78% and 21% of the atmosphere, respectively. The ratio of N_2 and O_2 is about 4:1. Above 100 km, O_2 sharply falls in density and disappears at about 200 km. This can be explained by the photodissociation of O_2 and the absence of turbulent mixing at that altitude [Kelly, 1989]. Above 250 km, the atomic oxygen (O) surpasses N_2 in density and becomes the dominant species. The density changes of O can also affect the plasma composition [Kelly, 1989].

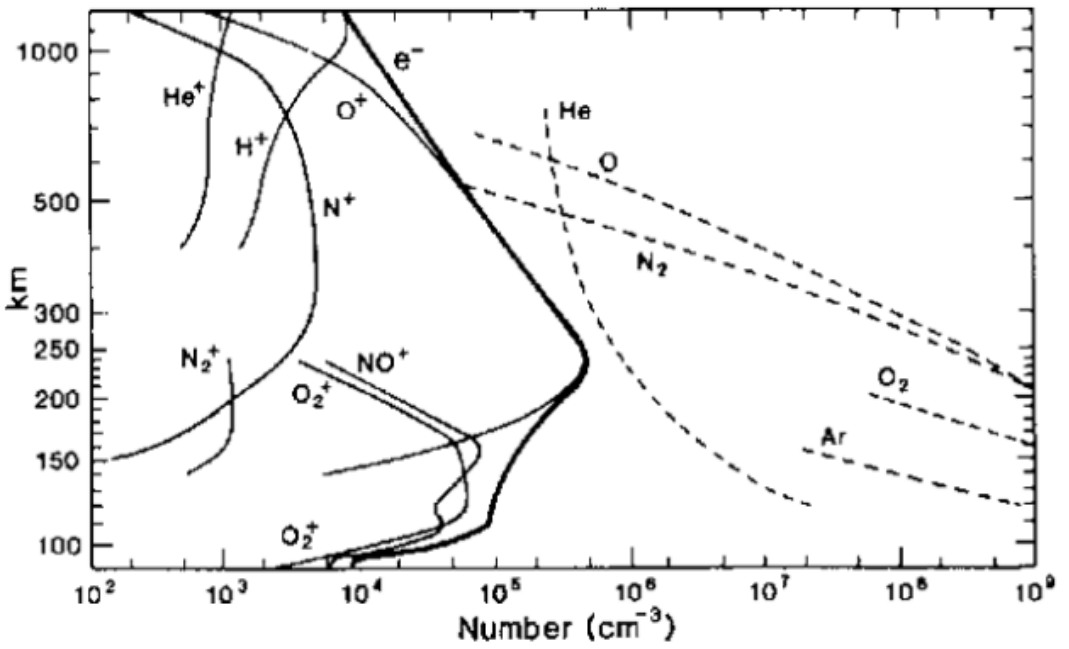

Figure 1.4 International Quiet Solar Year daytime atmospheric composition

https://malagabay.files.wordpress.com/2014/07/daytime-ionospheric-and-atmospheric-composition.gif

As shown in Figure 1.4, H^+ dominates the ion composition at altitude above 1000 km. The ions are almost all O^+ near the peak (200km-600km) of e^+, which is the electron density. This directly corresponds to the high density of atomic O at the same altitude. Below 200 km, NO^+ and O_2^+ become the most important components and dominate the ionosphere.

1.2.3 Main Layers of Ionosphere

Based on the intensity of plasma density, the ionosphere can be divided into three layers which named D, E and F layer from low altitude to high altitude. Figure 1.5 shows the ionospheric main layers during day and night.

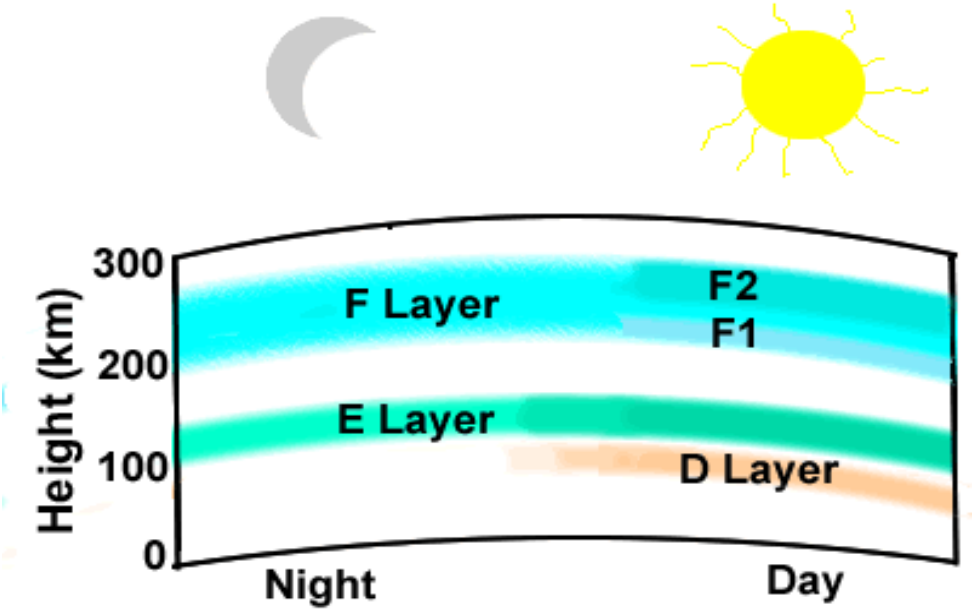

Figure 1.5 Daytime and nighttime ionospheric regions

https://upload.wikimedia.org/wikipedia/commons/4/49/IonosphereLayers-NPS.gif

From Figure 1.5, we can see during the nighttime, ionosphere only has two layers, E layer and F layer. During the daytime, because of the increased ionization by ultraviolet (UV) light and X-ray of the sun, ionosphere has some changes. F layer is divided into F_1 and F_2 layer (F_1 layer:150-210 km; F_2 layer: 210-500 km), E layer is significantly enhanced and a new layer (D layer) appears below E layer.

As the lowest layer of ionosphere, the D layer extends from about 60 km to 90 km. At this layer, the ionization is not very strong. NO^+ and O_2^+ which are ionized from N_2 and O_2 become the major ion components [Gong, 2012]. The altitude range 90 km- 150 km is designed as the E layer. The main ionization in this layer is O_2^+ and NO^+ ionized by the UV solar radiation and sun's X-ray. F layer, also called Appleton-Barnett layer, spreads from 150 km to 500 km or above. It is the top layer of the ionosphere and is also the densest region of the ionosphere. The

dominant ion in this layer is O^+, but with the increase of altitude (above 600 km), the number of O^+ gradually reduces and lighter ions like H^+ and He^+ become more dominant.

Chapter 2 F_3 layer, an additional layer

2.1 Introduction of the F_3 Layer

F_3 layer is an additional stratification of the F_2 layer. The F_3 layer can be recognized through two crests appearing above 210 km in the electron density profile [Zhao et al., 2011]. The first observation of the F_3 layer can be traced back to 1940s. In 1949, Hon Yung Sen published an article to describe this abnormal phenomenon of F_2 layer above Singapore, but at that time he couldn't give a reasonable explanation [Sen, 1949]. In 1997, this structure was named "F_3 layer" by Balan et al. and they and he also proposed a possible mechanism for F_3 layer [Balan et al., 1997]. After that, the F_3 layer received extensive investigations concerning its seasonal, diurnal and long term variations. Statistical data reveals that latitude 7° - 8° of the northern hemisphere and -7° - -8° of the southern hemisphere, longitude -160° - -170°, -80° - -100°, -20° - 20° and 80° - 120° are prone to the occurrence of the F_3 layer and it most commonly occurs during 10:00-14:00 LT in summer [Zhao et al., 2011].

Based on the theory of Balan et al[1998], the F_3 layer, which occurs during the daytime (about 8:30-14:00 LT) at low latitudes, are mainly caused by the upward **ExB** drift. Equatorward neutral wind also plays a minor role in the formation of F_3 layer. To put it simply, we can consider the magnetic field of the Earth as a dipole whose magnetic field points down toward the surface of the northern hemisphere and away from the southern hemisphere. In the F layer, the magnitudes of the gyro-frequency of electrons and ions are much larger than the corresponding collision frequency. These charged particles spiral around the Earth's magnetic field lines unless an electric field appears and makes the particles drift across the magnetic field line. The drift velocity equals to $\mathbf{E}x\mathbf{B}/B^2$. As the drift is caused by the electric field and the earth's magnetic field, we call it **ExB** drift or electrodynamic drift. Upward **ExB** drift can push the original F_2 layer up and at the same time a new layer can be formed at the position of the usual F_2 layer. At

first, the density of F_3 layer is greater than the density of the new F_2 layer. Both of them can be observed using a bottom-side ionosonde. Then F_2 layer and F_3 layer continue moving upward and the density of F_3 layer will reduce and the density of F_2 layer will increase. When the density of F_2 layer exceeds that of F_3 layer, topside-sounder can be used to detect the F_3 layer [Balan et al., 2008].

An electron density profile (EDP) at selected local time showing F_3 layer derived by the Arecibo ISR is exhibited in Figure 2.1.

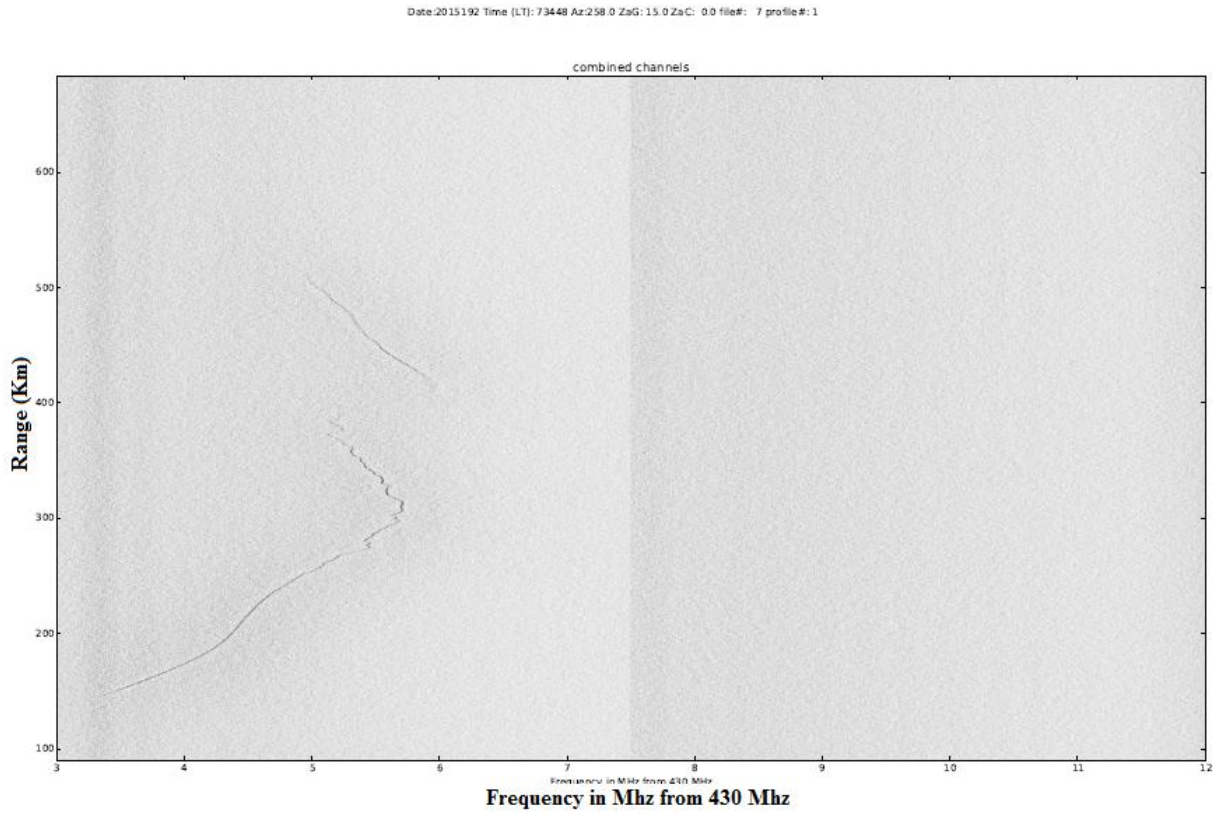

Figure 2.1 Electron density profile derived by Arecibo ISR

Time (LT): 7:21 Date: July 11, 2015 Az:258.0 Zag:15.0 Zac: 0.0

As shown in Figure 2.1, the black line represents the vertical distribution of electron density profile at 7:21 LT, July 11, 2015. At that time, the Arecibo dual-beam radar operated at 258° in azimuth. Linefeed antenna pointed vertically upward and Gregorian antenna pointed at 15° off zenith. We can clearly see two maxima exist in the electron density profile. One peak intensity altitude is around 300 km, the other one is around 420 km. This is a typical sign of F_3 layer. But it occurred at early morning, which falls outside the typical window (8:30-14:00 LT)

of F_3 layer occurrence reported by Balan et al [1998]. In the following sections, this rare F_3 layer will be discussed and analyzed in more detail.

2.2 Data Analysis

In this thesis, about 2 days of incoherent scatter radar were taken at Arecibo. For data recorded from 20:20 LT July 10 to 6:30 LT July 11 and 16:00 LT July 11 to 6:35 LT July 12, the azimuth angle of Arecibo ISR cyclically rotated from 80° to 180° (0° represents north, 90° represents east and 180° represents west). For data recorded from 6:45 LT to 15:55 LT July 11, and 6:45 LT to 16:00 LT July 12, the azimuth angle of Arecibo ISR was at 258°. For all the 6 periods, the Linefeed antenna was pointed at 0° zenith angle and the Gregorian antenna was pointed at 15° zenith angle.

2.2.1 Determine the Electron Density

A typical ISR spectrum (Figure 2.3) consists of a double humped ion line and two plasma lines which are symmetrically distributed on both sides of the transmitter frequency, F_T. The plasma line frequency is directly related to the electron density.

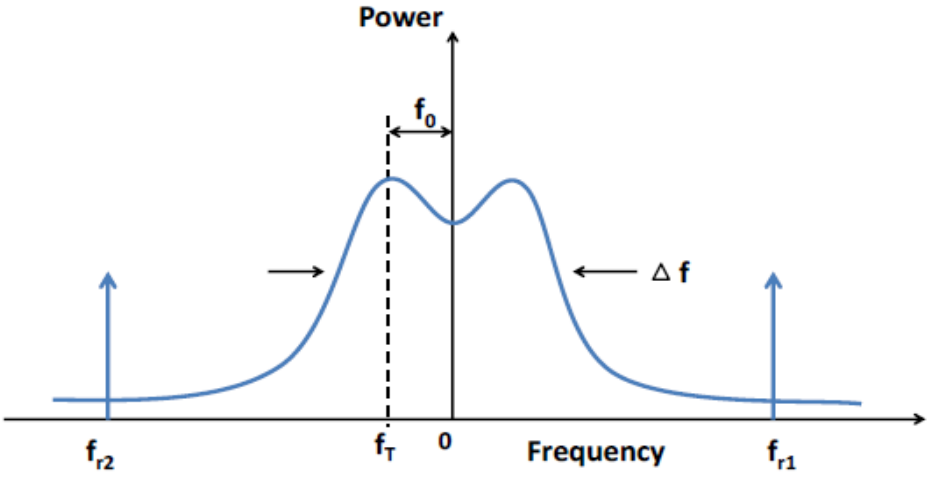

Figure 2.2 Incoherent Scatter Spectrum [Gong, 2012]

In Figure 2.2, the horizontal axis represents frequency and vertical axis represents power. The Doppler shift f_0 equals $-2V/\lambda$. Where V is the bulk velocity of the plasma and λ is the radar wavelength. Δf is the width of the IS spectrum and it is mostly determined by the ion and

electron temperatures as well as ion mass. f_{r1} represents the up-shift plasma line and f_{r2} represents the down-shift plasma line.

There are two traditional ways to determine electron density (Ne) as a function of height. One is to derive Ne from the ion line, another is from plasma line. For the "ion line" method, the area under the ion line curve expresses the total power and it is proportional to the plasma density.

The total power at altitude h is equal to:

$$K\sigma N_e / h^2 = K\sigma_e \sin^2 \gamma N_e /(1+T_e / T_i)h^2 \tag{2.1}$$

where $\sigma = \sigma_e (1+T_e / T_i)^{-1}$, K is a system constant which is related to the transmitted power and the effective area of the antenna. γ represents the angle between the magnetic field and the radar beam. We can calculate Ne, if we know Te/Ti.

For the "plasma line" method, if the Debye length is much less than the radar wavelength, the electron density can be determined from the frequency offset of the plasma line [Beynon and Williams, 1978]. The relationship of plasma frequency (f_p) and electron density (Ne) can be shown as:

$$f_p = \sqrt{\frac{N_e e^2}{m^* \varepsilon_0}} \times 2\pi, [Hz] \tag{2.2}$$

where e is the electric charge, m^* is the effective mass of the electron, and ε_o is the permittivity of free space. The "plasma line" method is more accurate than the "ion line" method, but it can only be applied during the daytime for Ne determination because the plasma lines are too weak to be detected at night. Figure 2.3 shows Ne derived by plasma line on July 11 and July 12.

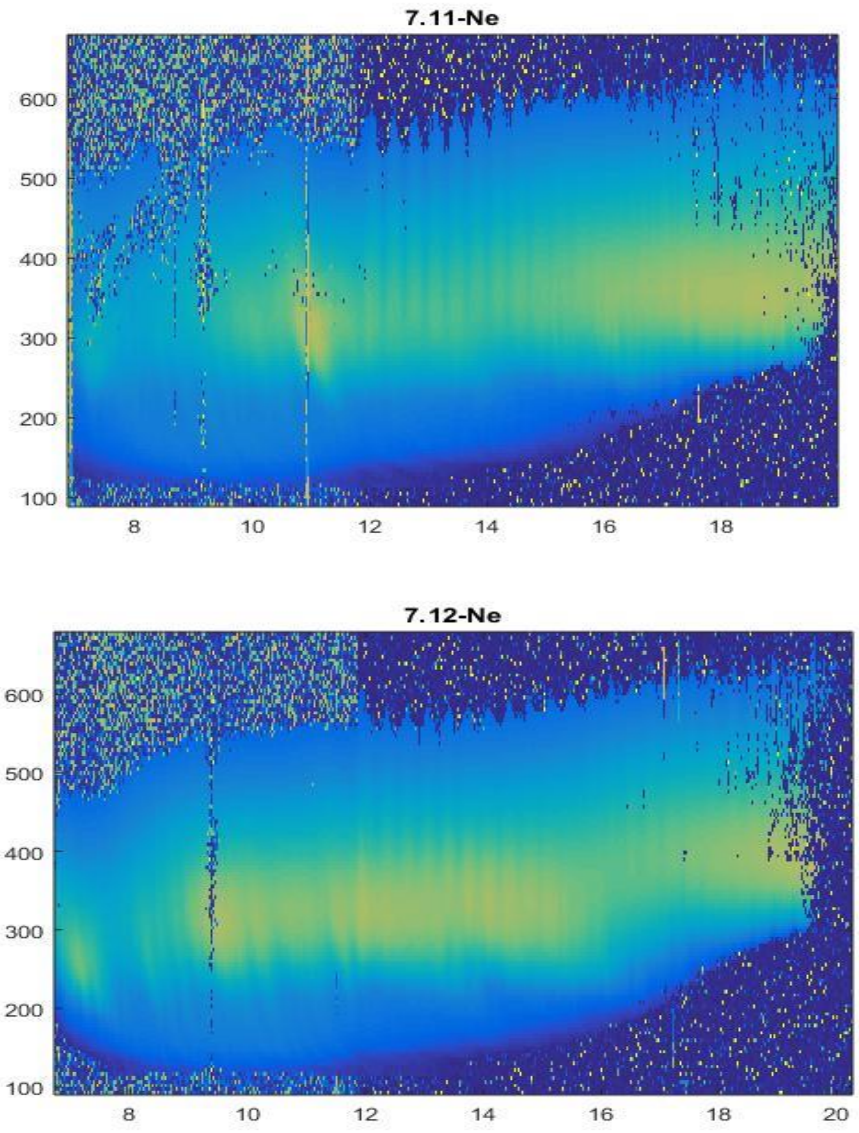

Figure 2.3 Ne of July 11 and July 12 measured from plasma line

Abnormal Ne existed at altitude from 300 km to 550 km during about 6 :30 LT to 9:00 LT in July 11. It is easy to see the differences between the day of the F_3 layer phenomenon (July 11) and the day without F_3 layer phenomenon (July 12). The electron density determined by the "ion line" method from Gregorian beam and linefeed beam for two days are shown in Figure 2.4. Comparing Figure 2.3 and Figure 2.4, we can easily see Ne derived from ion line is not as accurate as that derived from the plasma line, but abnormal Ne region from 300 km to 550 km at early morning of July 11 still can be observed.

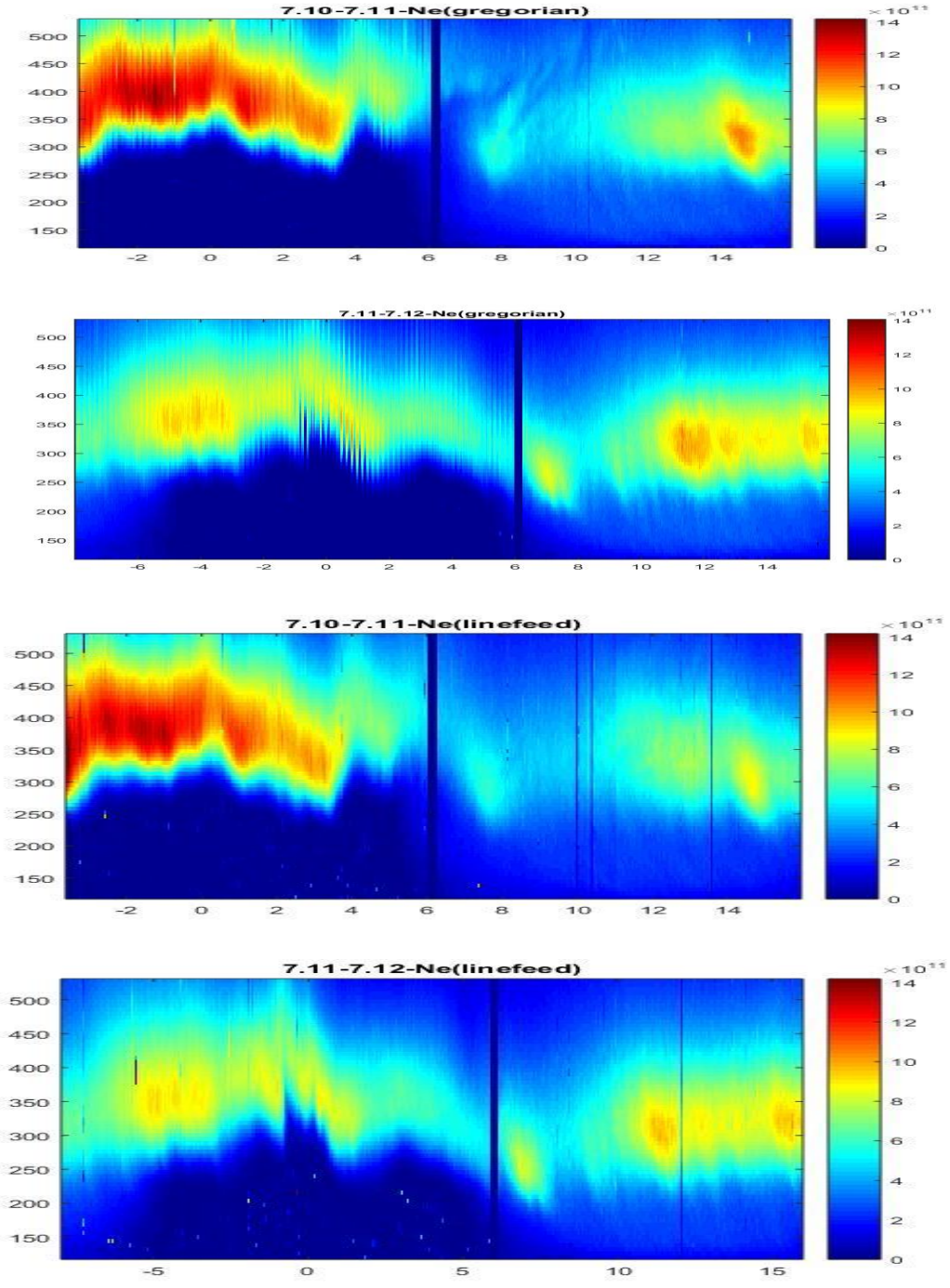

Figure 2.4 Electron density derived from Gregorian and Linefeed

2.2.2 Electron Density Profile (EDP)

As shown in Figure 2.5, Figure 2.5 (a) and (b) show the EDP derived by the Gregorian beam and the Linefeed beam of July 11. Figure 2.5 (c) and (d) show the EDP derived by Gregorian beam and Linefeed beam of July 12.

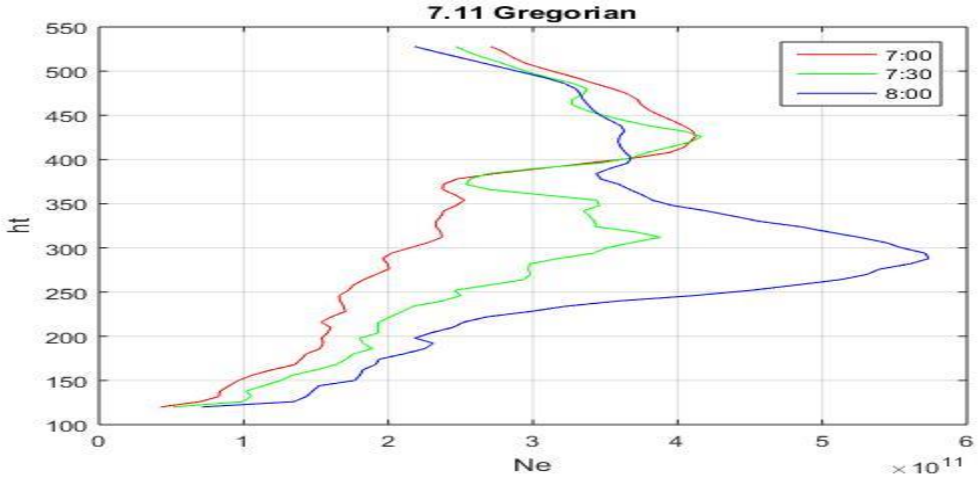

Figure 2.5(a) EDP derived by Gregorian beam, July 11

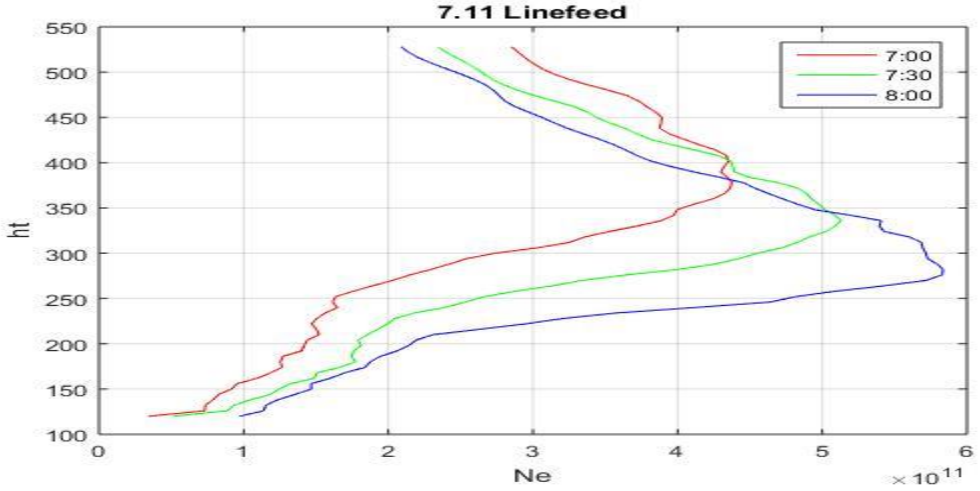

Figure 2.5(b) EDP derived by Linefeed beam, July 11

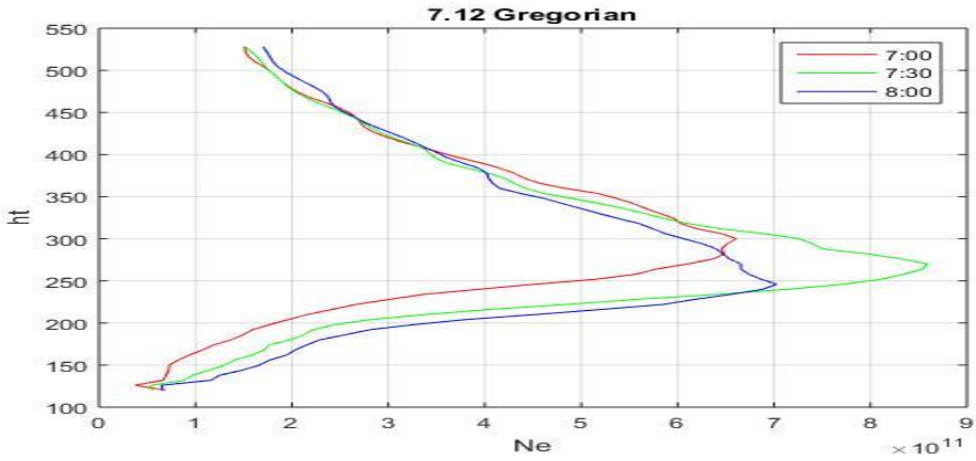

Figure 2.5(c) EDP derived by Gregorian beam, July 12

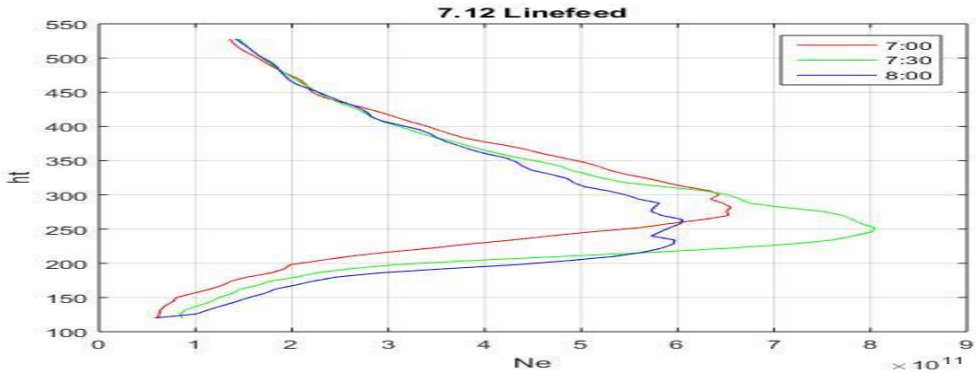

Figure 2.5(d) EDP derived by Linefeed beam, July 12

Compared with the EDP derived at specific local times of different days and different beams, only Gregorian feed recorded the F_3 layer phenomenon in the early morning of July 11. The F_3 layer started to form at about 7:00 am, LT. At that time, electron density at 430 km of July 11was about 4.2e11 m^{-3}. At about 7:30 LT, the Ne of the F_2 layer was approximately equal to the Ne of the F_3 layer, which was 4.0e11 m^{-3}. This moment was the best time to observe the double-crest, then the F_3 layer weakened but still existed for about half an hour and the F_2 continued to strengthen. At about 8:00 LT, F_3 layer went away and the only crest appeared at about 270km. The Ne was about 5.8e11 m^{-3}.

2.2.3 Ne Horizontal Inhomogeneity

If the F_3 layer phenomenon is due to uplifting of the F_2 layer uniformly, we should see double peaks in the Linefeed as well. As shown in Figure 2.5 (b), at 7:00 LT there is only one crest at about 380 km altitude and the maximum electron density is about 4.2e11 m^{-3}. At 8:00 LT, the crest drops to about 280 km and the value increases to about 5.8e11 m^{-3}. Vertical **ExB** drift can make the peak shifting, but cannot make the peak increasing. The maximum peak value at 8:00 LT is much than that at 7:00 LT. The increase in the peak value is due to the increased solar radiation. As shown in Figure 2.5 (a), the Linefeed didn't record the F_3 layer during 7:00 LT to 8:00 LT, July 11. The absence of a F3 layer in the vertical direction indicates horizontal inhomogeneity must exist.

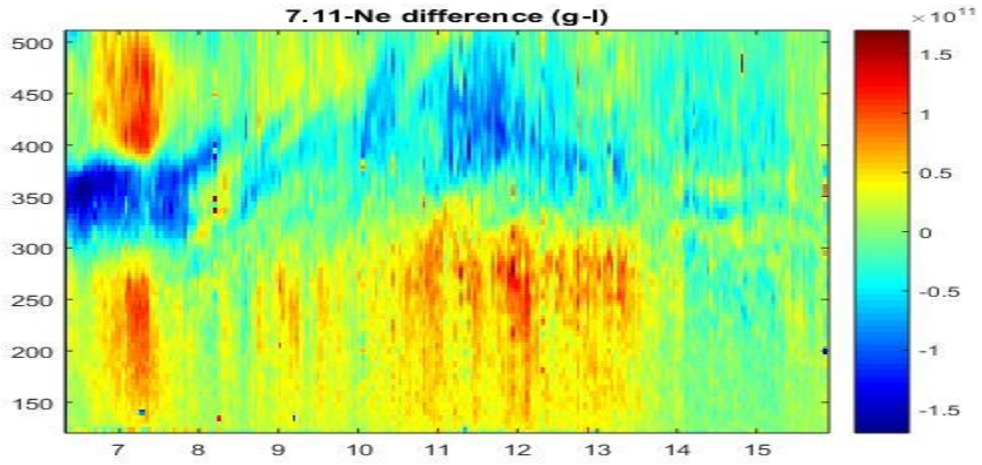

Figure 2.6(a) Ne difference plot between the two feeds, July 11

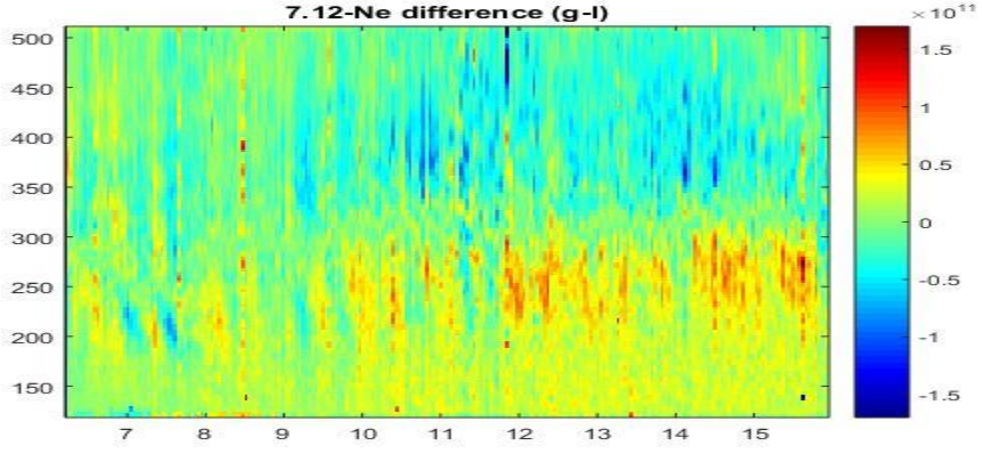

Figure 2.6(b) Ne difference plot between the two feeds, July 12

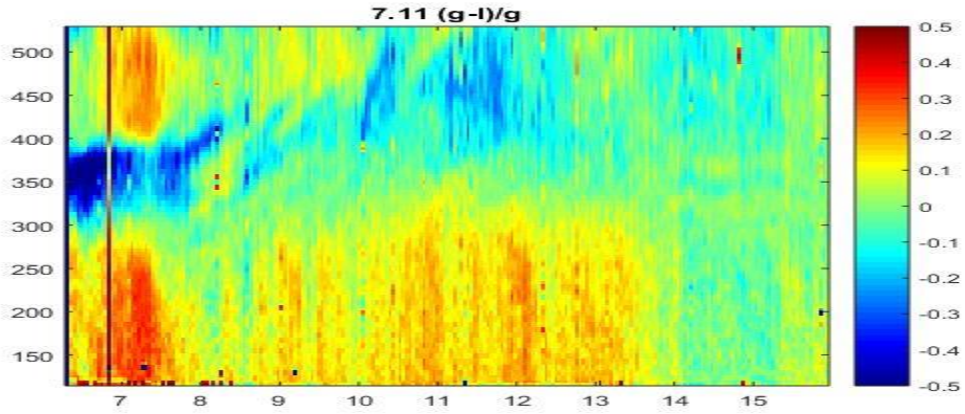

Figure 2.6(c) Normalized Ne difference between the two feeds, July 11

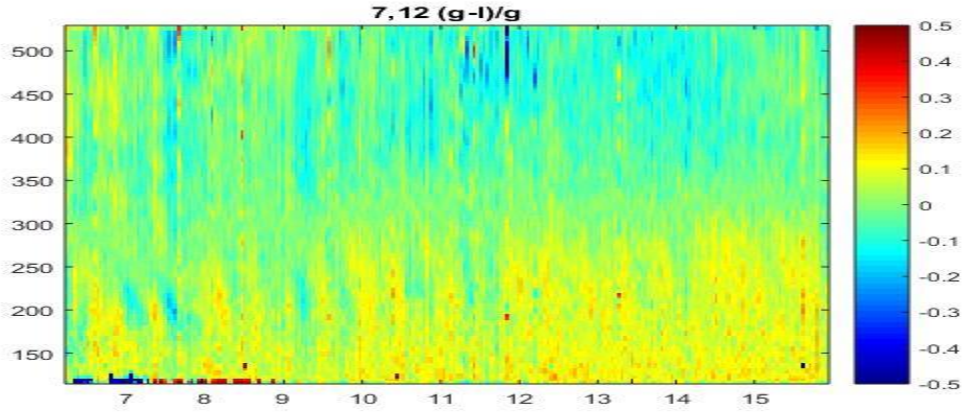

Figure 2.6(d) Normalized Ne difference between the two feeds, July 11 to July 12

According to Figure 2.6 (a) and (c), Ne difference is 1e11 to 1.5e11 electrons m^{-3} at altitude 320 km to 380 km during about 6:30 LT to 8:00LT in July 11. This density difference indicates electrons in Gregorian feed area is less than 30 to 50 percent of the electrons in the Linefeed area. Compared to the Figure 2.6 (c) and (d), when F_3 layer is not existence, there is no Ne difference between Gregorian feed and Line feed. The reasoning for this abnormal F_3 layer is that ionospheric Ne exists horizontal inhomogeneity between the Gregorian feed and the Linefeed. Comparing the Ne from the Linefeed and Gregorian feed at 7:30 LT on July 11 suggests that the double peak in the Gregorian peak is not a density enhancement. It is in fact a decrease in electron density at 350 km. Because of the short horizontal scale involved and the large electron density difference between the

Linefeed and Gregorian feed, horizontal gradient is the most important role in the formation of F_3 layer in our observation.

Chapter 3 Nighttime Horizontal Gradient Analysis

3.1 Nighttime Ne Difference

3.1.1 Ne difference

From the chapter above, we know the horizontal gradient is the main reason for the formation of the F_3 layer in the Gregorian feed. The analysis of the ionosphere condition before the occurrence of the F3 layer gives us the context of the occurrence of the F3 layer. This chapter focuses on the variations of the ionospheric horizontal gradient at nighttime. In Figure 3.1, we show the difference in electron density for the nights of July 11 and July 12. It should be noted the Gregorian feed moved back and forth between 70 to 180 degrees azimuth angle at a zenith angle of 15 degrees. Each swing takes a few minutes. The Linefeed was pointed in the vertical direction all the time. The fluctuation in the Ne difference plots is associated with the azimuth motion of the Gregorian feed.

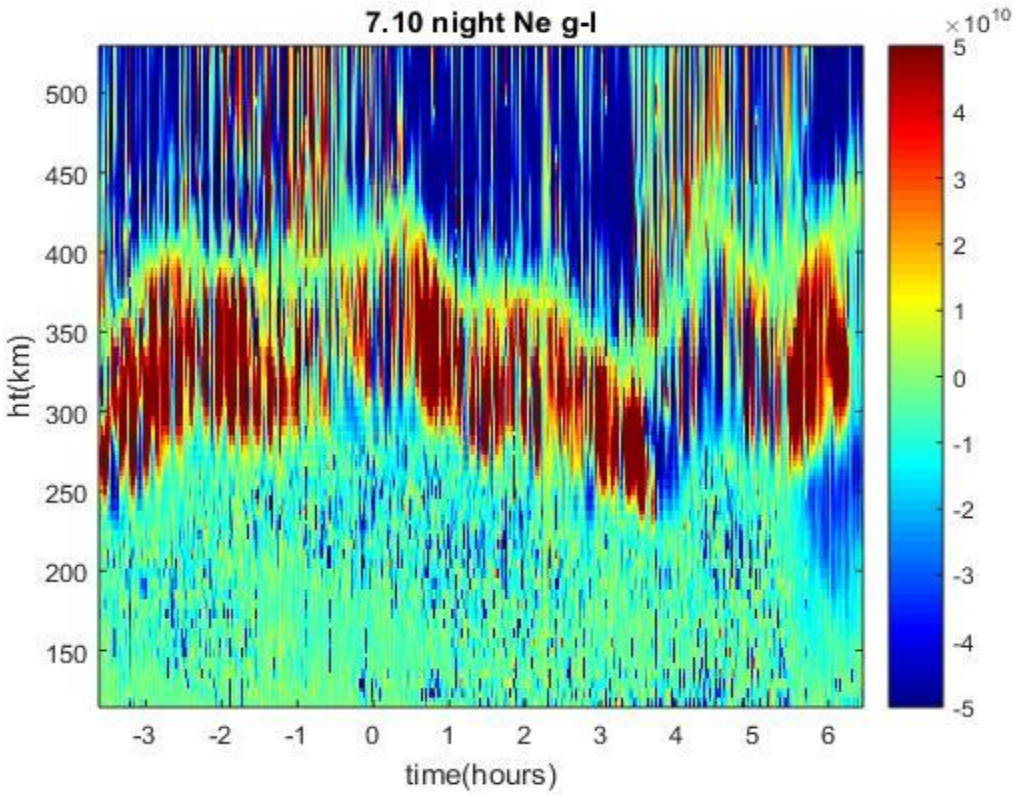

Figure 3.1 (a) Ne difference plot between two feeds, nighttime of July 10

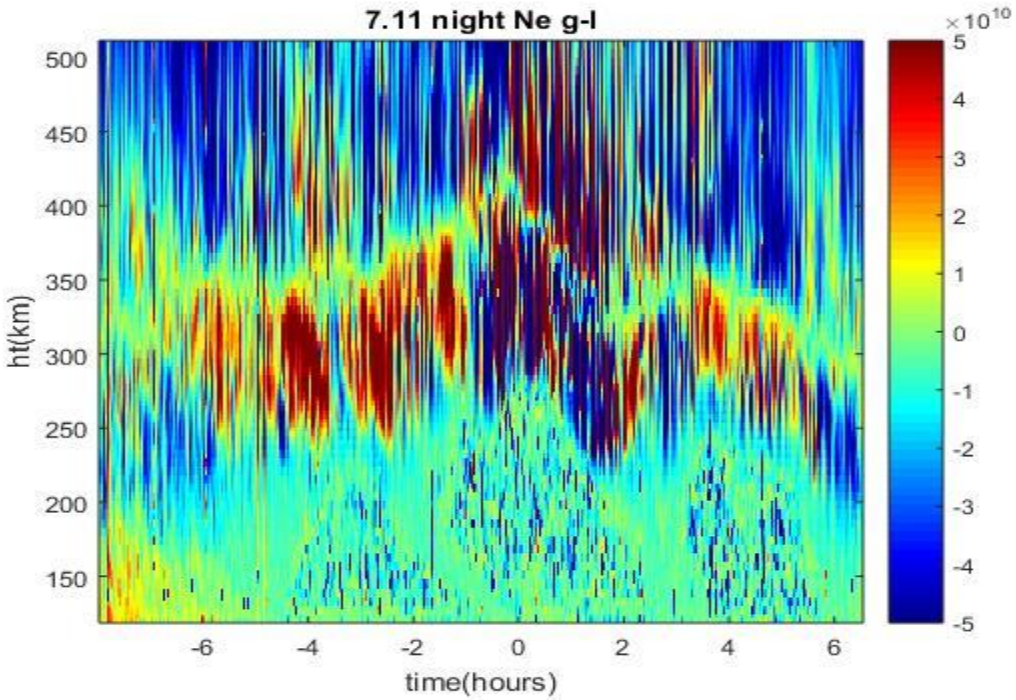

Figure 3.1 (b) Ne difference plot between two feeds, nighttime of July 11

For both Ne difference plots (July 10 and July 11), we can see they have a wavy green band (same electron density in the two feeds) at about 250 km to 400 km almost through nighttime. For fields above the wavy bands, Ne in Gregorian feed is lower than that in the Linefeed, which suggests Ne has a smaller gradient above 400 km. For fields below the wavy bands, gradient is close to zero, and Ne in the Gregorian feed and Line feed has the same value most of the time. For Ne difference plot of July 10, Ne in Gregorian feed is less than it in Linefeed during 4:00 LT to 5:00LT. For Ne difference plot of July 11, the wavy band started at about 18:00 LT, July 10 and ended at about 5:30 LT, July 11. During 0:00 LT to 2:00 LT, the Ne is extremely unstable and the horizontal gradient changed drastically.

3.1.2 Electron Density Profile

Figure 3.1 (a) can be divided into three broad time intervals according to the Ne difference characteristics. These intervals are 21:00 LT of July 10 to 4:00 LT of July 11, 4:00 LT of July 11 to 5:00 LT of July 11 and 5:00 LT of July 11 to 6:45 LT of July 11. Figure 3.2 (a), (b) and (c) denote representative EDP derived by the Gregorian beam and the Linefeed beam at 21:17 LT of July 10, 4:10 LT of July 11 and 6:01 LT of July 12 respectively.

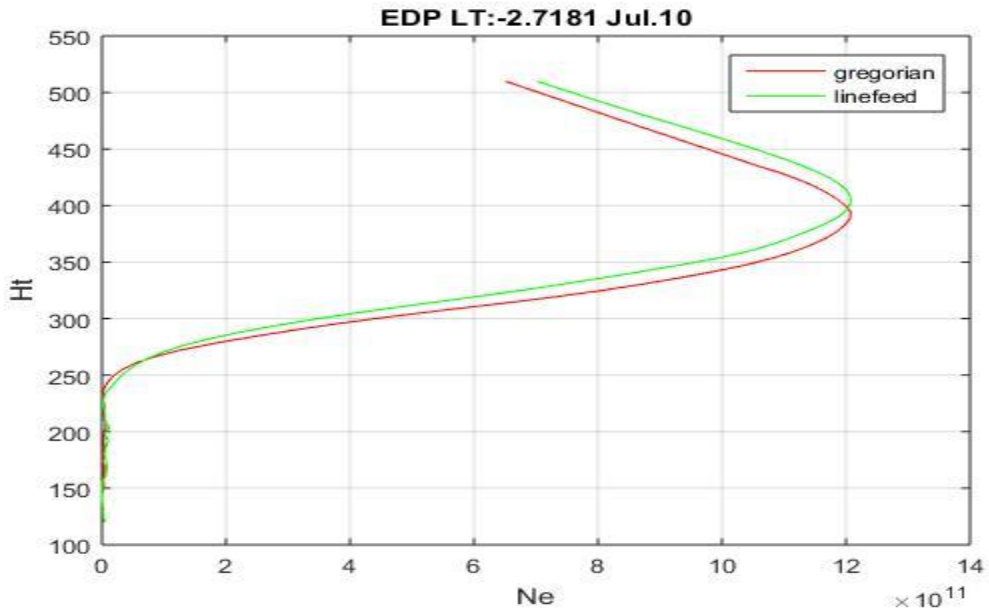

Figure 3.2 (a) EDP, 21:17 LT on July 10

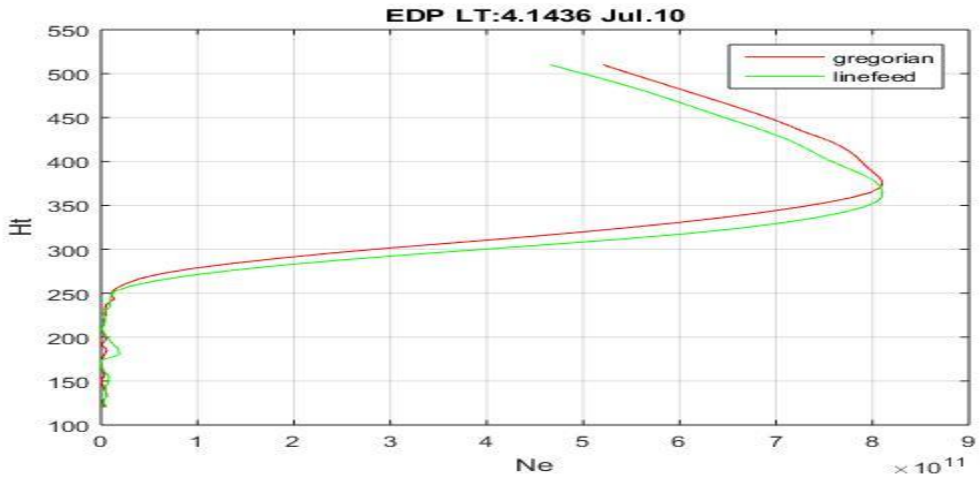

Figure 3.2 (b) EDP, 4:10 LT on July 11

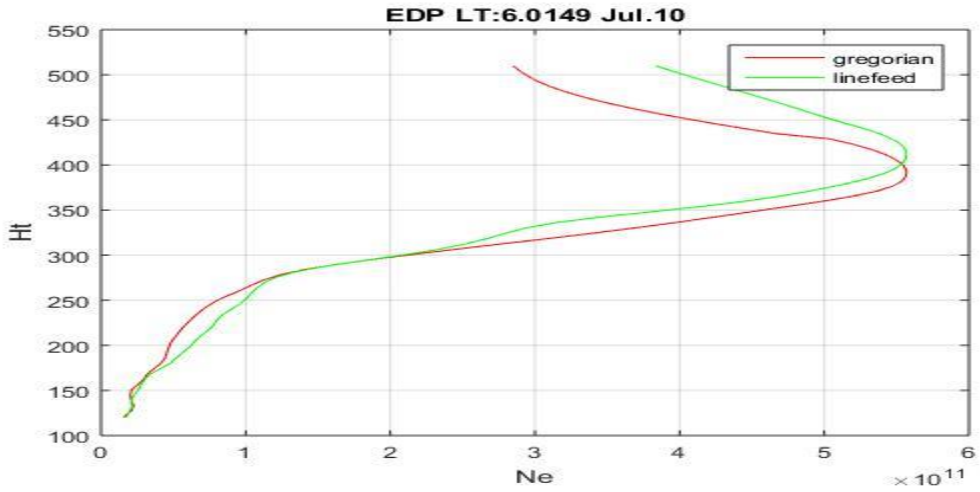

Figure 3.2 (c) EDP, 6:01 LT on July 11

Figure 3.2 (a) represents typical electron distribution during 21:00 LT of July 10 to 4:00 LT of July 11. The EDP is derived at 21:17 LT. Red curve represents Ne in Gregorian and green curve represents Ne in Linefeed. Above 400 km, the green curve is above the red curve, i.e., the Linefeed Ne is larger than that of the Gregorian feed. The value of the Gregorian feed is larger than that of the Linefeed from 230 km to 400 km. This corresponds to the red wavy band in Figure 3.1 (a). Ne in Gregorian is larger than that in Linefeed. Below 230 km, both Ne values of the Gregorian feed and the Linefeed are very small and at the same level. The horizontal gradient is close to zero below 230km.

Figure 3.2 (b) is a typical example of EDP during 4:00 LT of July 11 to 5:00 LT of July 11. Above 370 km, the Ne value of the Gregorian feed is larger than that of the Linefeed. From

230 km to 370 km, the Ne value of the Gregorian feed is less than that of the Linefeed. As in Figure 3.1 (a), Ne difference above 370 km is positive and Ne difference during 230 to 370 is negative and Ne difference below 230 is close to zero during 4:00 LT to 5:00 LT, July 11. What this indicates is that there is strong horizontal inhomogeneity throughout the F-region.

Figure 3.2 (c) is more complex, above 400 km the situation is the same as Figure 3.2 (a). From 280 to 400 km, Ne in the Gregorian feed is larger than that in the Linefeed, but from 150 km to 280 km, the opposite is true. As shown in Figure 3.1 (a), there is some blue areas after 5:00 LT from 150 km to 280 km altitude, indicating that the Gregorian Ne is lower than that of the Linefeed.

We do the same EDP analysis for the night of July 11th in Figure 3.3. Figure 3.1 (b) can be divided into 4 broad bands, which correspond to 18:00 LT to 23:00 LT on July 11, 23:00 LT of July 11 to 4:00 LT of July 12, 4:00 LT to 5:30 LT on July 12 and 5:30 LT to 6:45 LT of July 12. Figure 3.3 (a), (b), (c) and (d) denote EDPs derived by the dual beams at 21:54 LT on July 11, 3:10 LT,4:19 LT and 6:22 LT on July 12 respectively to represent Ne difference of these 4 bands. During 23:00 LT of July 11 to 4:00 LT of July 12, the Ne difference changed drastically. From 5:30 LT of July 12 to 6:45 LT of July 12, as shown in Figure 3.3 (d), the value of the Linefeed is always larger or equal to that of the Gregorian feed, which shows that the gradient during that time is always negative or close to zero.

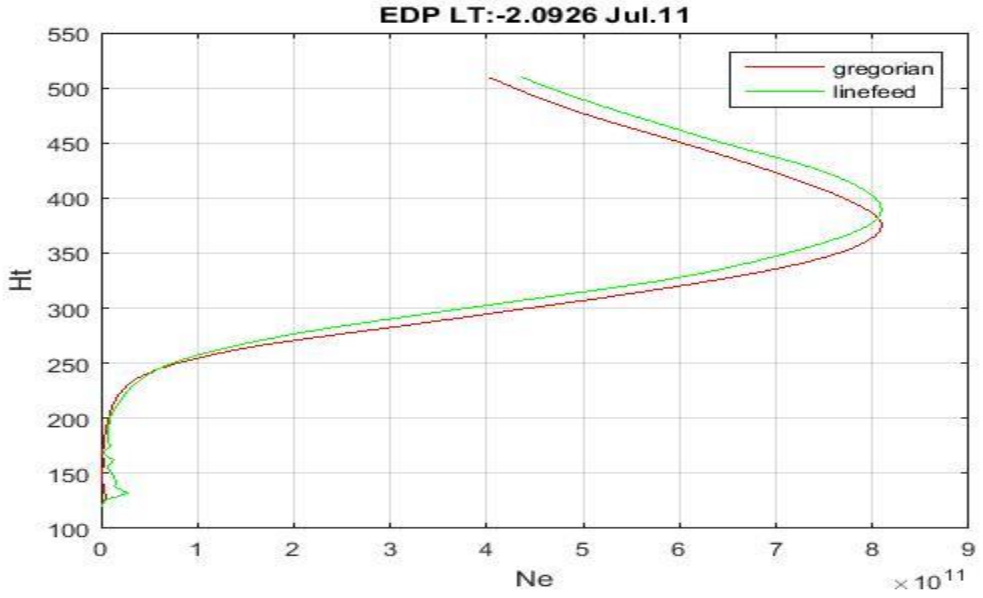

Figure 3.3 (a) EDP, 21:54 LT on July 11

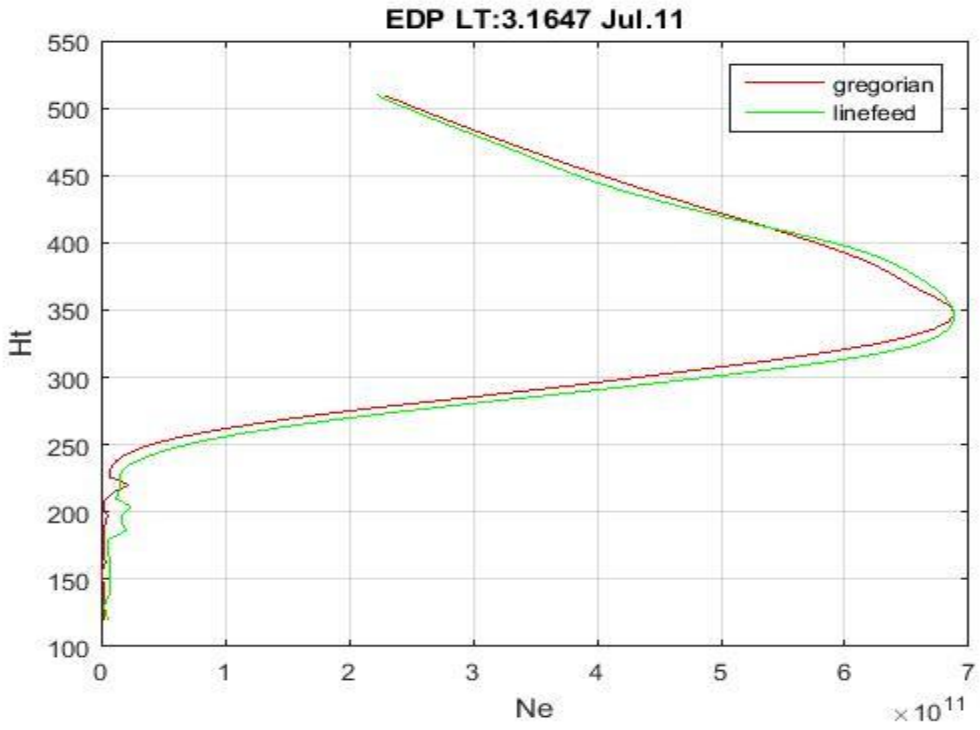

Figure 3.3 (b) EDP, 3:10 LT on July 12

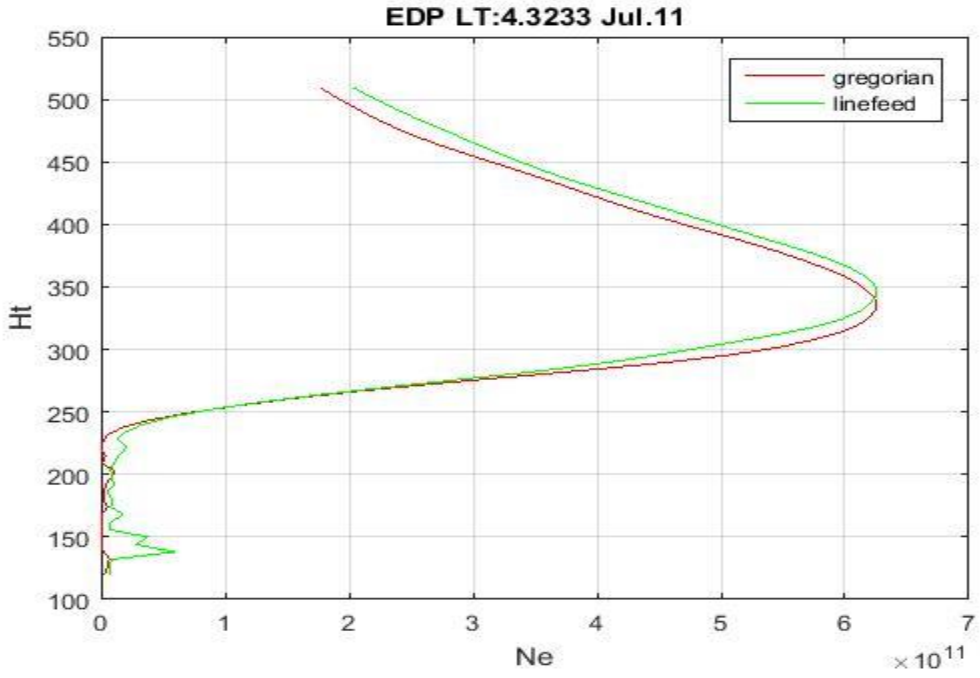

Figure 3.3 (c) EDP, 4:19 LT on July 12

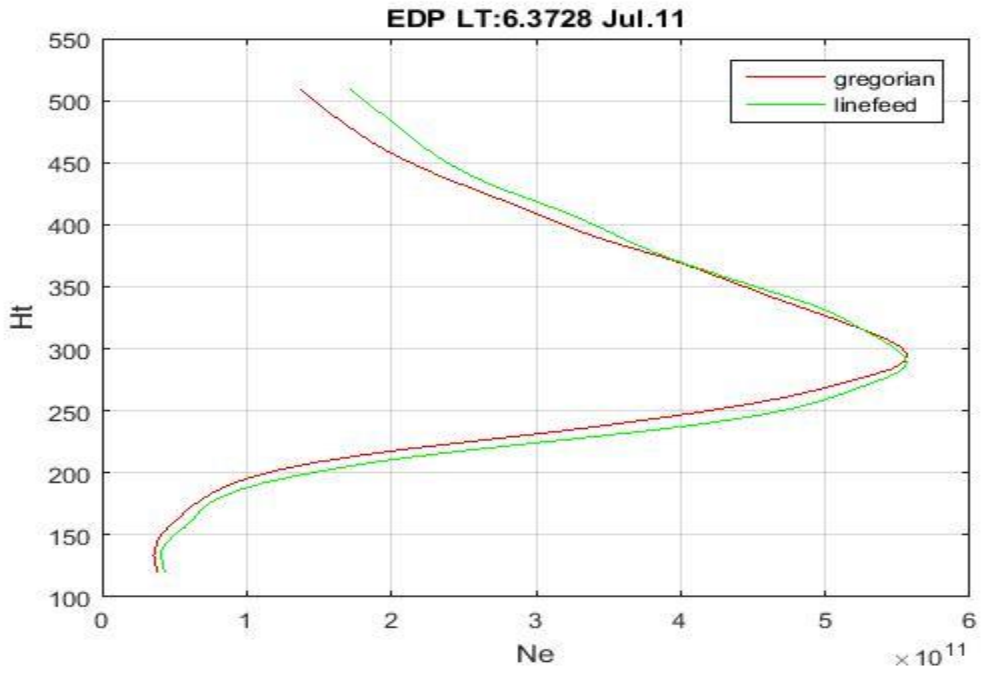

Figure 3.3 (d) EDP, 6:22 LT on July 12

3.2 Horizontal Gradient Direction Analysis

3.2.1 Horizontal Gradient of Different Altitude

Gregorian feed was pointed at 258° azimuth angle during the daytime. At nighttime the Gregorian feed rotated constantly back and forth between 70° to 180° (0° represents north, 90° represents east and 180° represents south). The variation of the azimuth angle on July 11 and July 12 is shown in Figure 3.4. The sampling region of the Gregorian feed is an arc surface, instead of a line at nighttime. Because of the rotating nature of the beam configuration, we can calculate the horizontal gradient between the linefeed and the Gregorian feed at different altitudes.

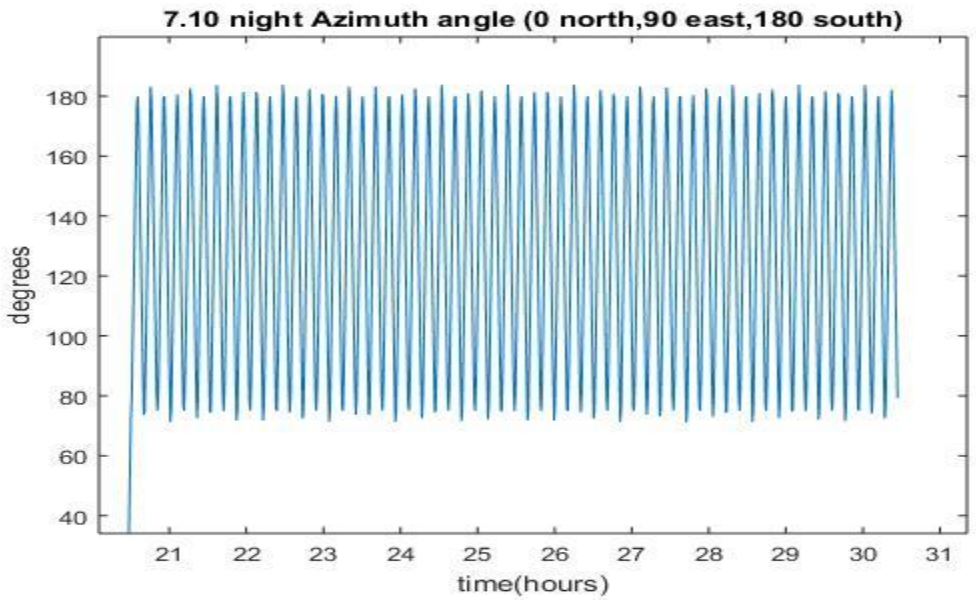

Figure 3.4 (a) Variation of azimuth angle, nighttime July 10

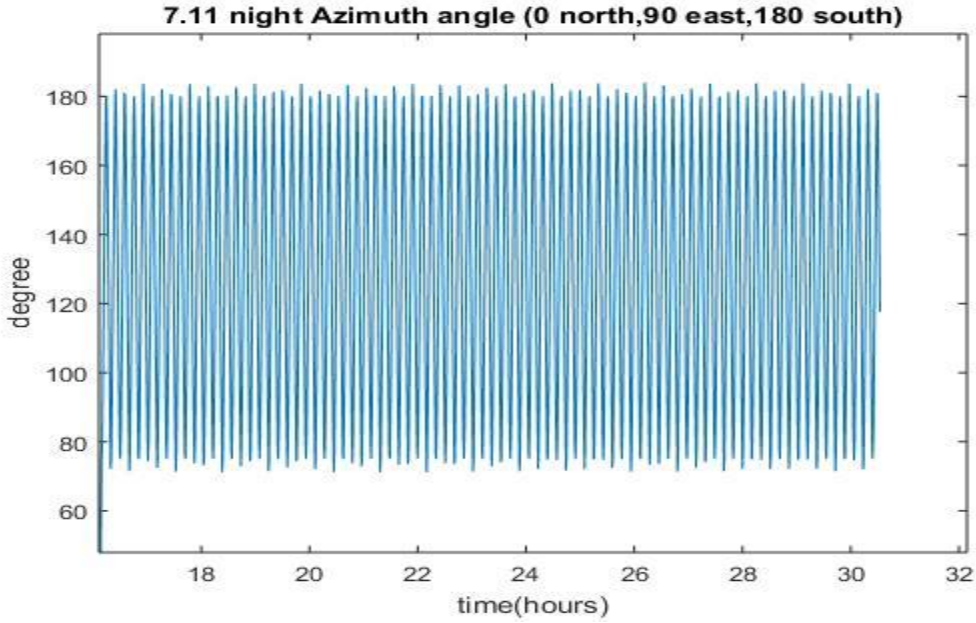

Figure 3.4 (b) Variation of azimuth angle, nighttime July 11

As shown in Figure 3.4 (a) and (b), the Gregorian feed rotated 114 cycles on the night of July 10 and it rotated 166 cycles at night of July 11. The range of motion in each cycle is from 70° to 180° azimuth angle for both nights or from 180° to 70°. The Following figures show the horizontal gradient at different altitudes.

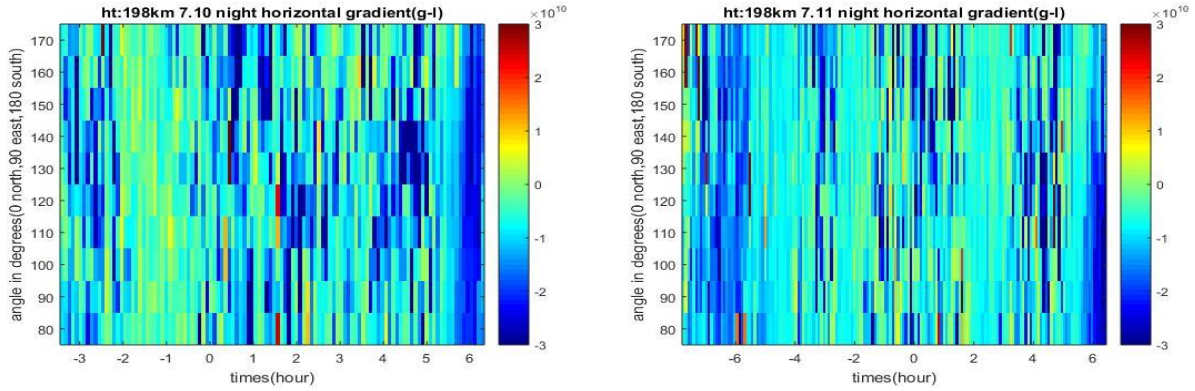

Figure 3.5 (a) Horizontal Ne difference between the Gregorian feed and the Linefeed at 198 km altitude, nighttime of July 10 (left) and July 11 (right)

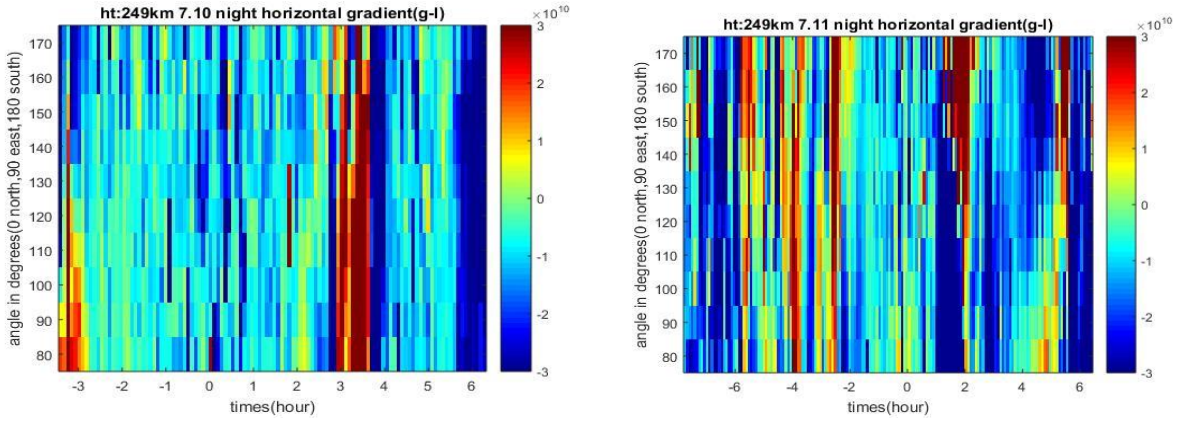

Figure 3.5 (b) Horizontal Ne difference between the Gregorian feed and the Linefeed at 249 km altitude, nighttime of July 10 (left) and July 11 (right)

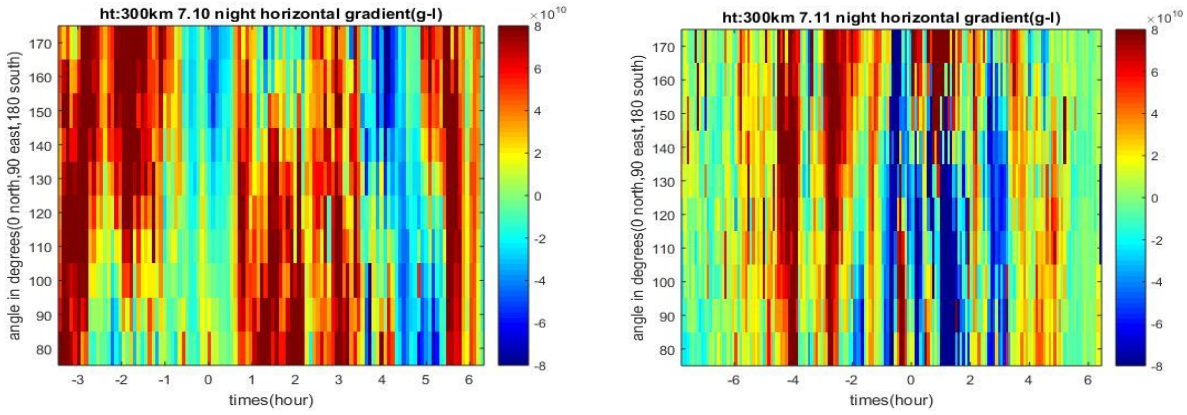

Figure 3.5 (c) Horizontal Ne difference between the Gregorian feed and the Linefeed at 300 km altitude, nighttime of July 10 (left) and July 11 (right)

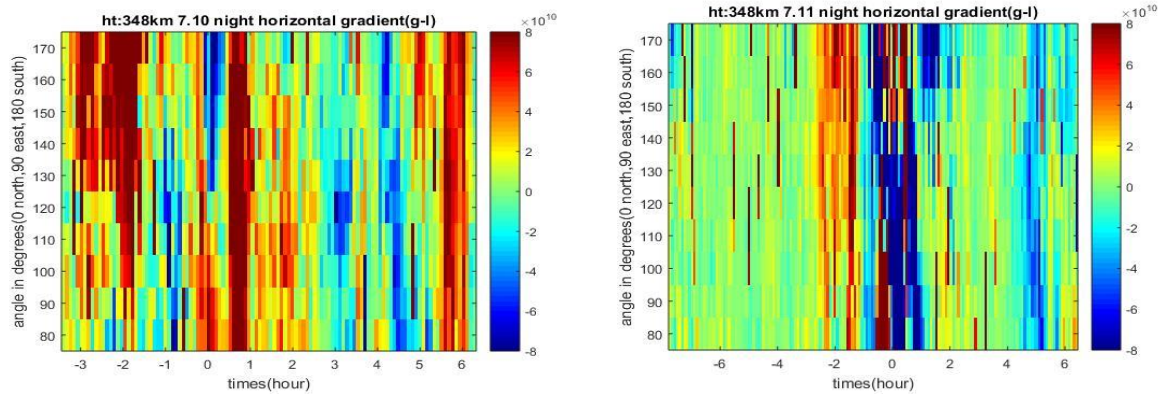

Figure 3.5 (d) Horizontal Ne difference between the Gregorian feed and the Linefeed at 348 km altitude, nighttime of July 10 (left) and July 11 (right)

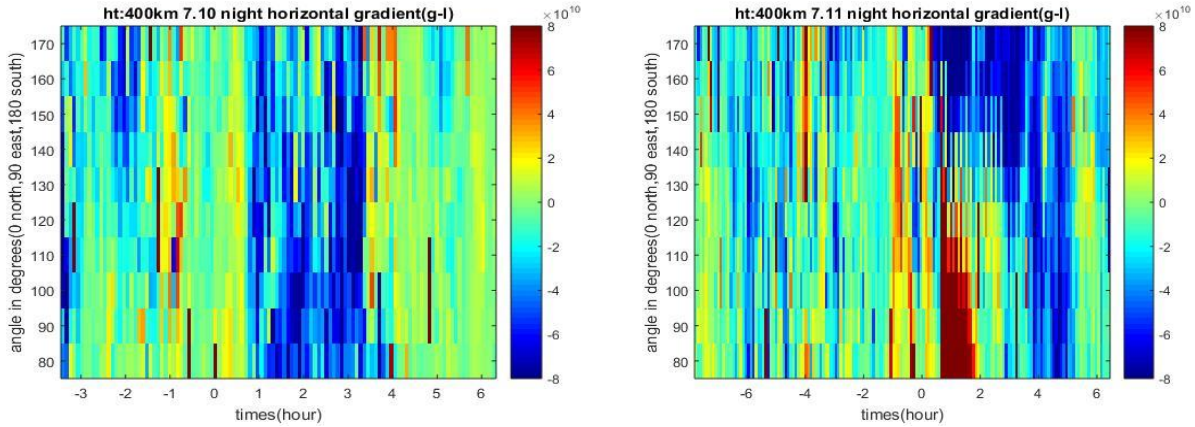

Figure 3.5 (e) Horizontal Ne difference between the Gregorian feed and the Linefeed at 198 km altitude, nighttime of July 10 (left) and July 11 (right)

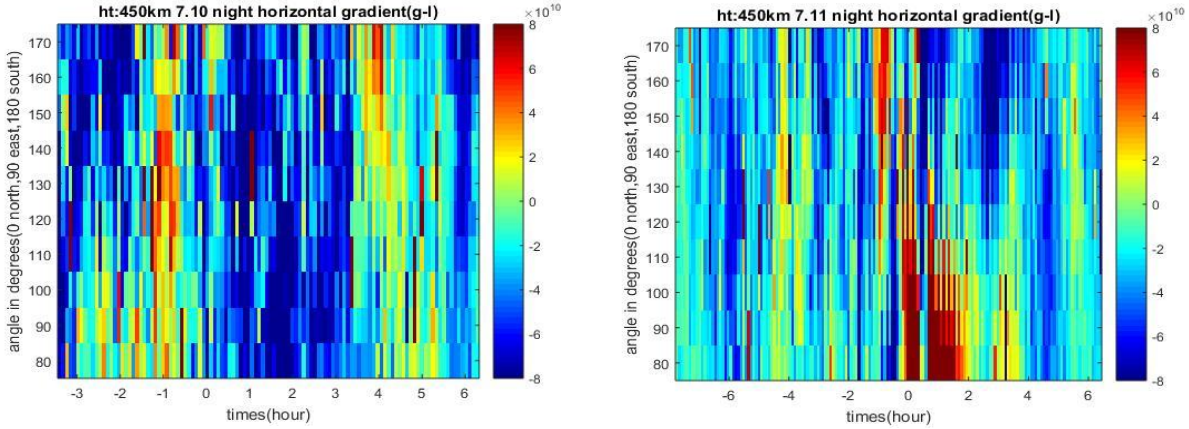

Figure 3.5 (f) Horizontal Ne difference between the Gregorian feed and the Linefeed at 198 km altitude, nighttime of July 10 (left) and July 11 (right)

In Figures 3.5, we plot the Ne difference between the Gregorian feed and the Linefeed. The horizontal axis represents times and the vertical axis represents azimuth direction. In Figure 3.5 (a), at 198 km altitude, Ne difference (Gregorian minus Linefeed) is equal or less than zero for all time, which shows that the electron density in Linefeed always equal or larger than Gregorian in any direction (70° to 180°). In Figure 3.5 (b), at 249 km altitude, Ne difference is about 3e10 m^{-3} during 3:00 LT to 3:45 LT from azimuth angle 70° to 160° at night of July 10. Ne difference is about 3e10 m^{-3} during 3:00 LT to 3:45 LT from azimuth angle 135° to 180° at night of July 11. For the rest of the nighttime, Ne difference is equal to or less than zero. In figures 3.5 (c) and (d), Ne difference is larger than zero for most of the time. The Ne at the Gregorian section is larger at 300 km and 348 km altitude. In the left panel of Figure 3.5 (e), Ne difference range is from 0 to 3e10 m^{-3} during 21:00 LT to 1:00 LT and 4:00 LT to 6:20 LT. During 1:00 LT to 4:00 LT of July 11, the horizontal gradient is negative. For the right panel in Figure 3.5 (e), during 0:30 to 2:00 LT of July 12, Ne difference is about 8e10 m^{-3} from azimuth angle 70° to 110°. For Figure 3.5 (f), Ne difference is negative or equal to zero for most of the time at 450 km altitude. Summarizing the above information, the electron density of the Gregorian feed is larger than that of the linefeed from 250 km to 400 km altitude. The horizontal difference is less than or equal to zero for most cycles above 400 km and below 250 km. Positive difference means that Ne in the south-east direction is larger than that in the center. These conclusions can also be seen in Figure 3.1 (a) and (b). The red wavy bands appear at about 250 km to 400 km, which means electron density in Gregorian dominates over that in Linefeed at that altitude range.

3.2.2 Horizontal Gradient Normal Direction Analysis

The ionospheric horizontal gradient could be obtained from empirical models updated with real time data [Nagarajoo, 2012]. In this section, we introduce a simplified method to estimate the horizontal gradient normal direction between Gregorian and Linefeed in the peak altitude of the F_2 layer.

Figure 3.6 (a) and (b) show the variations of maximum ionization height (hmf_2) and azimuth angle of the two nights, July 10 and July 11. Blue curve represents hmf_2 derived from the Linefeed, green curves represent hmf_2 derived from the Gregorian feed.

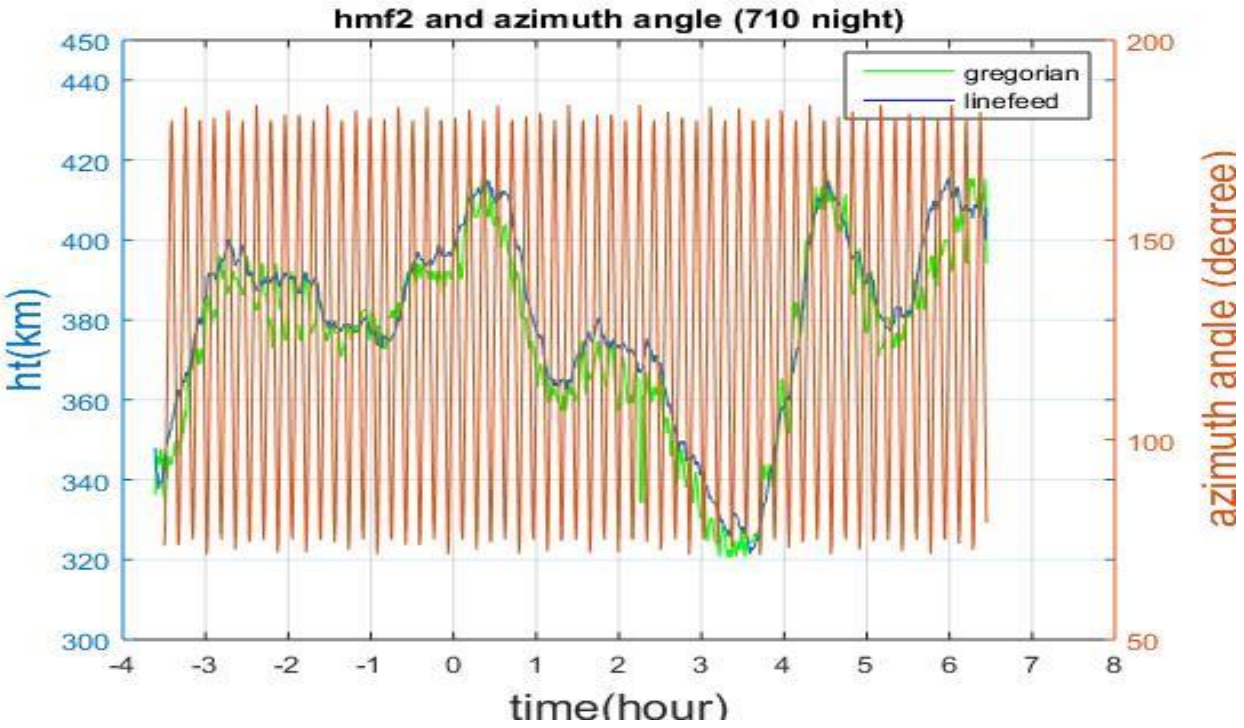

Figure 3.6 (a) Hmf_2 and azimuth angle, nighttime July 10

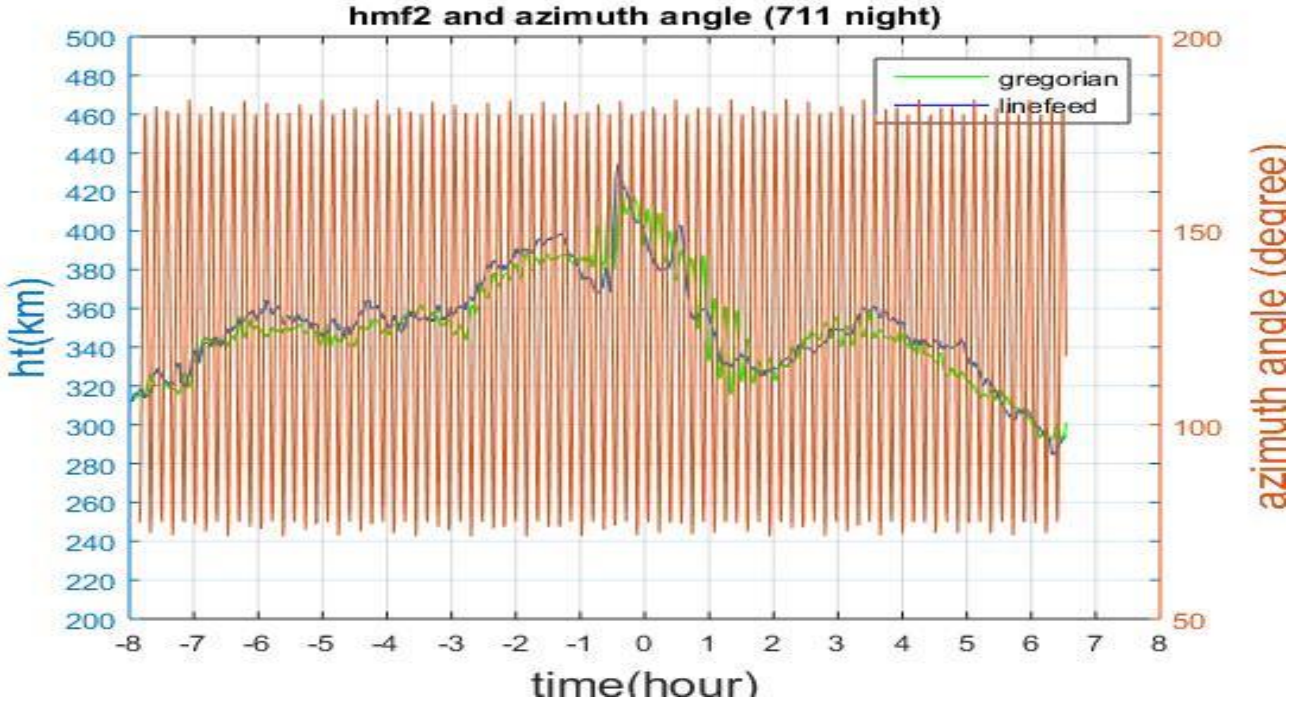

Figure 3.6 (b) Hmf_2 and azimuth angle, nighttime July 11

From Figure 3.6, we can see the variation of the Gregorian hmf_2 is the same as that of the Linefeed. In Figure 3.6 (a) and (b), we can observe midnight collapse phenomenon (i.e., a sharp drop in hmf_2) shortly after midnight [Gong, 2012]. This is a typical phenomenon for nighttime ionosphere above Arecibo [Zhou et al., 1997]. The hmf_2 curves dropped about 80 km from about 0:00 LT to 3:00 LT.

Incorporating blue curves and green curves at same cycle, we can roughly calculate the horizontal gradient normal direction. For example, the azimuth angle corresponding to the largest difference between Gregorian and Linefeed is approximately the horizontal gradient normal direction. If the two curves have an intersection point, Ne in Gregorian and Linefeed have the same hmf2. Then we can derive the iso-hmf2. The normal direction of the hmf2 gradient should be perpendicular to the iso-hmf2 line. Through the analysis of the available information, we can estimate the ionospheric tilt direction during nighttime. Figure 3.7 shows the hmf2 gradient normal direction for the nights of July 10 and July 11.

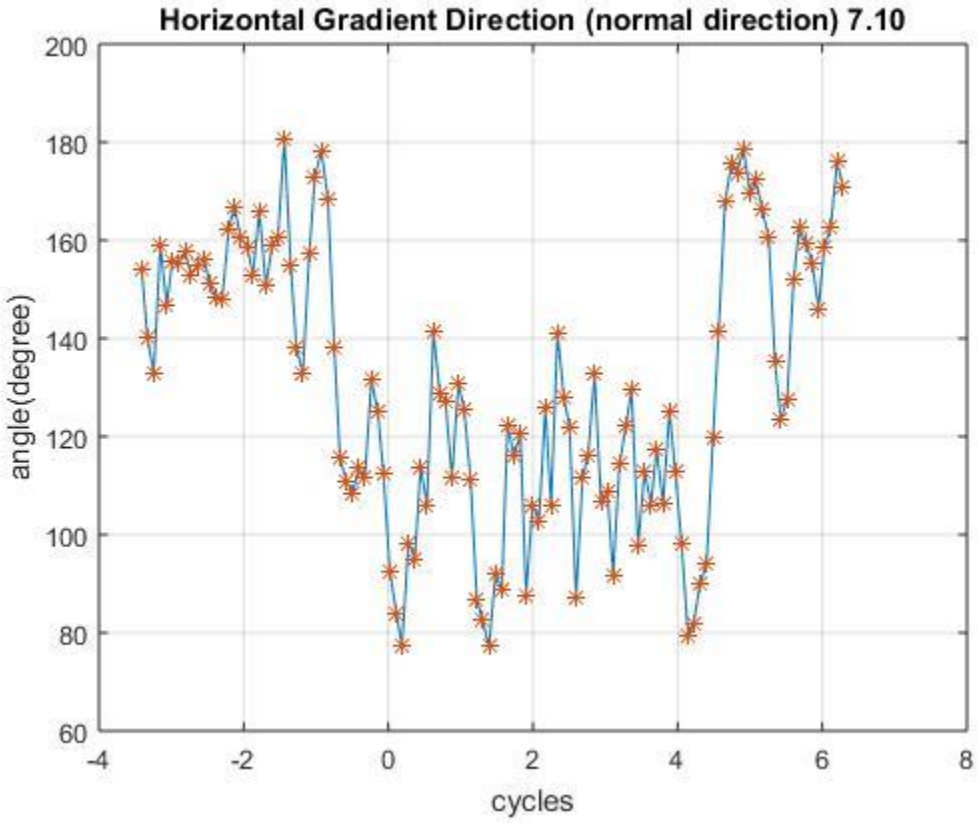

Figure 3.7 (a) Horizontal Gradient Direction, nighttime July 10

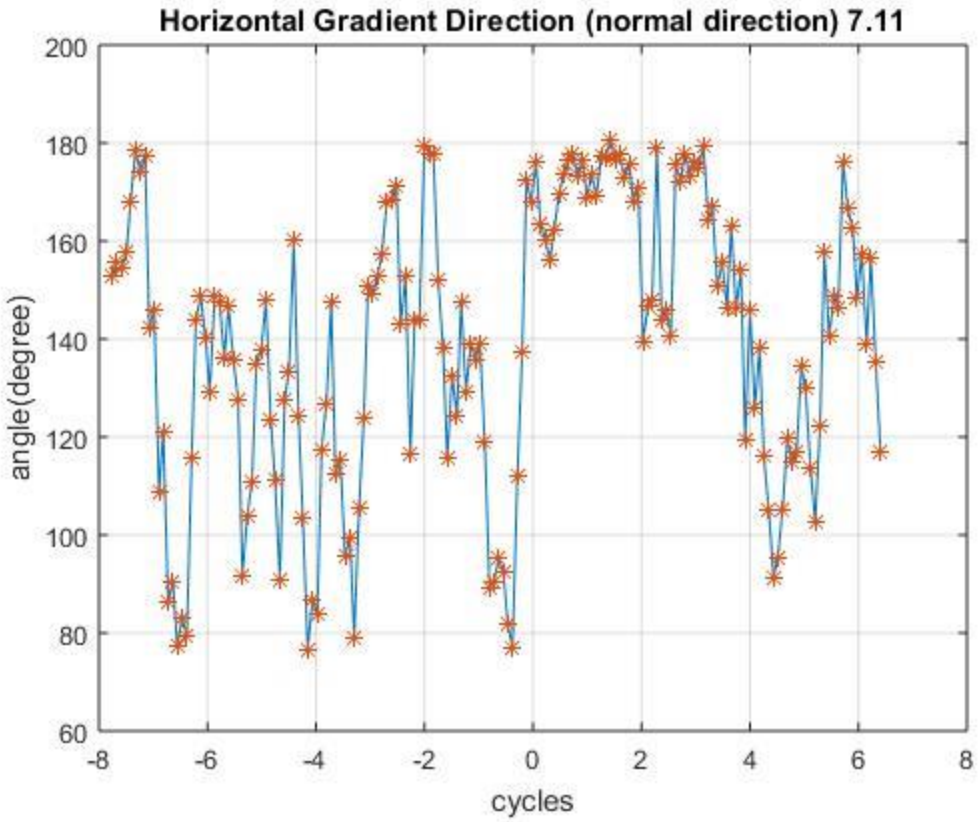

Figure 3.7 (b) Horizontal Gradient Direction, nighttime July 11

In Figure 3.7 (a) and (b), the horizontal axis represents time and the vertical axis represents the normal direction. 180°, for example, means that hmf_2 in south and 90° means that hmf_2 is highest in east direction. On the night of July 10^{th}, the horizontal gradient direction fluctuated between 135° to 180° before 23:00 LT of July 10. Then the gradient normal direction dropped to about 100° azimuth angle and fluctuated between 90° to 130° from the 23:00 LT of July 10 to 4:00 LT of July 11. After 4:00 LT of July 11, the range of gradient normal direction is 130° to 170° azimuth angle. On the night of July 11, the horizontal gradient direction fluctuated between 80° to 180° before 0:00 LT of July 11. Then it stabilized at about 170° from 0:00 LT of July 12 to 4:00 LT of July 12. After 4:00 LT of July 12, the horizontal gradient normal direction decreased to 90°, then increased to 180° and then decreased to 120° azimuth angle.

Chapter 4 Observation of Electron and Ion Temperature

Heating, cooling, and energy flow are the three main factors to determine the ionospheric temperature [Schunk and Nagy, 1978]. The solar radiation reaching into the atmosphere can cause ionization of neutral atoms and generate photoelectrons, then the photoelectrons can transmit their energy to ambient electrons. A series of these processes can cause the rising of electron temperature and ion temperature [Bardhan et al., 2015]. In this section, we present the electron temperature, ion temperature as well as their ratio. In particular, we want to see whether the temperatures or the temperature ratio are changed during the occurrence of the F3 layer.

4.1 Te and Ti analysis

Electron temperature (Te) and ion temperature (Ti) can strongly affect the ionosphere by controlling many physical and chemical processes [wang et al., 2012]. To illustrate the relationship between the variation of Te and the F_3 layer, we present four plots in Figure 4.1. Figure 4.1 (a) and (b) show variation of Te during 20:00 LT on July 10 to 17:00 LT on July 11 and during 17:00 LT on July 11 to 17:00 LT on July 12. Figure 4.1 (c) and (d) show variation of Ti during the two periods.

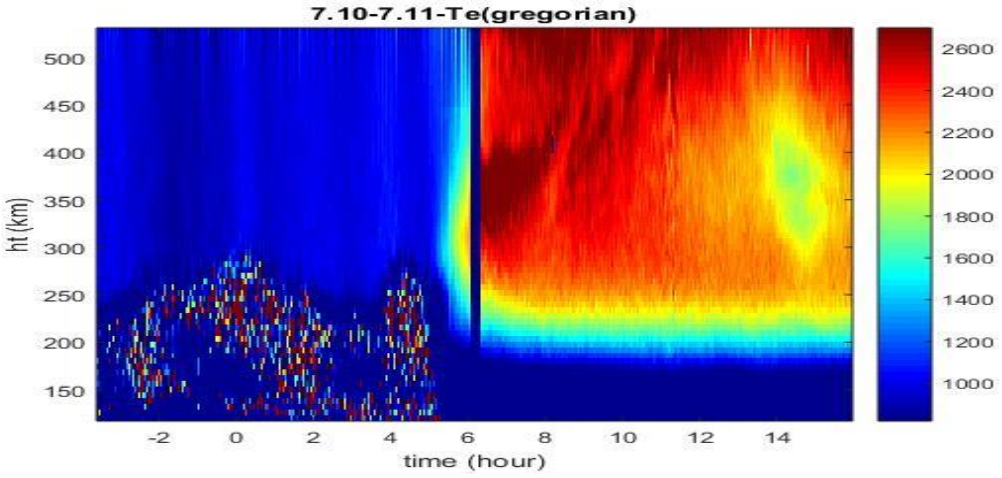

Figure 4.1(a) Variation of Te during July 10 to July 11

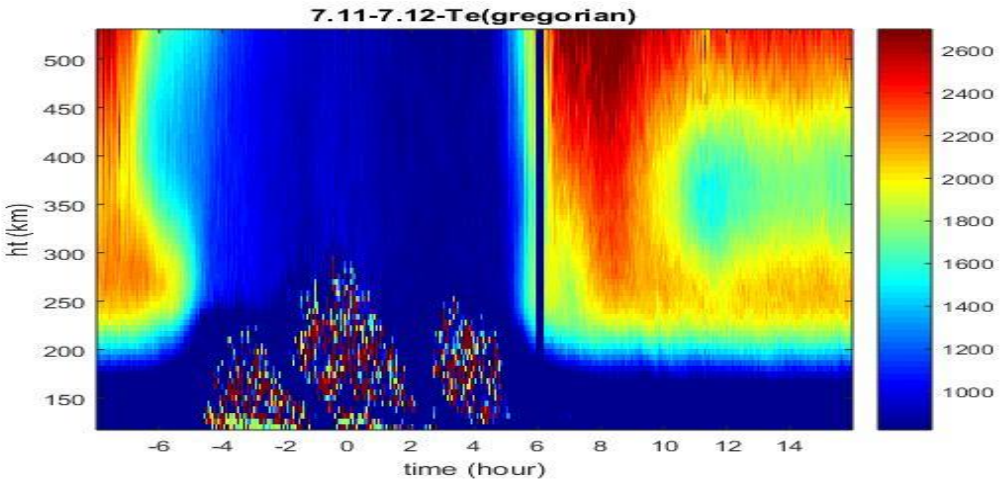

Figure 4.1(b) Variation of Te during July 11 to July 12

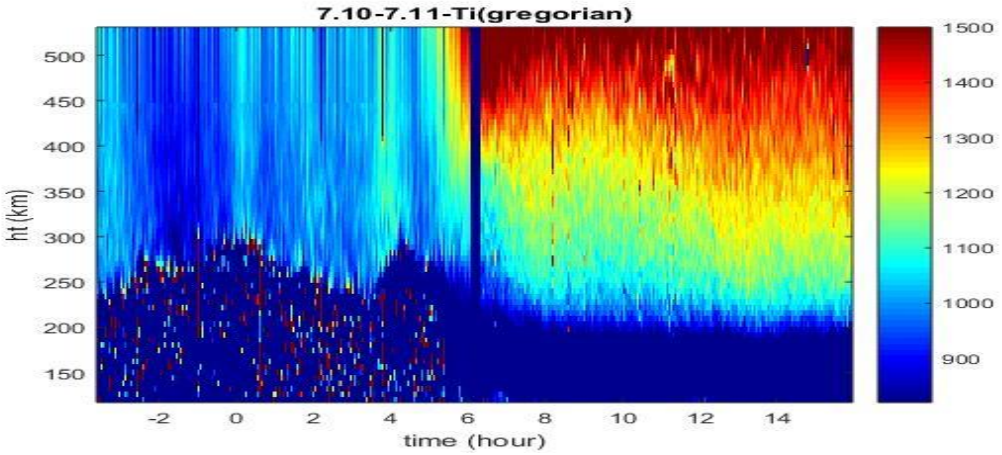

Figure 4.1(c) Variation of Ti during July 10 to July 11

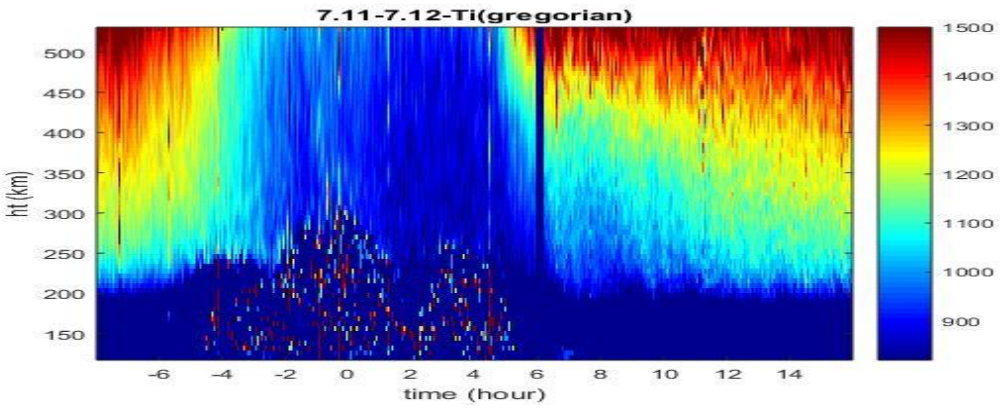

Figure 4.1(d) Variation of Ti during July 11 to July 12

For all the above figures, we can see that Te and Ti increase at the sunrise and decrease at the sunset. Te and Ti are on a high temperature level during daytime and this is related to the ionization of neutrals by solar radiation [Bardhan et al., 2015]. Comparing Figure 4.1 (a) and (b), Te increases to a higher temperature at altitude 300 km to 550 km during about 6:30 LT to 9:00 LT in July 11 when the F_3 layer appeared. Comparing Figure 4.1 (c) and (d), show that Ti of July 10 night has a higher temperature level than that of July 11. To illustrate the phenomenon clearly, Figure 4.2 shows variation of Te and Ti at 350km of these two periods.

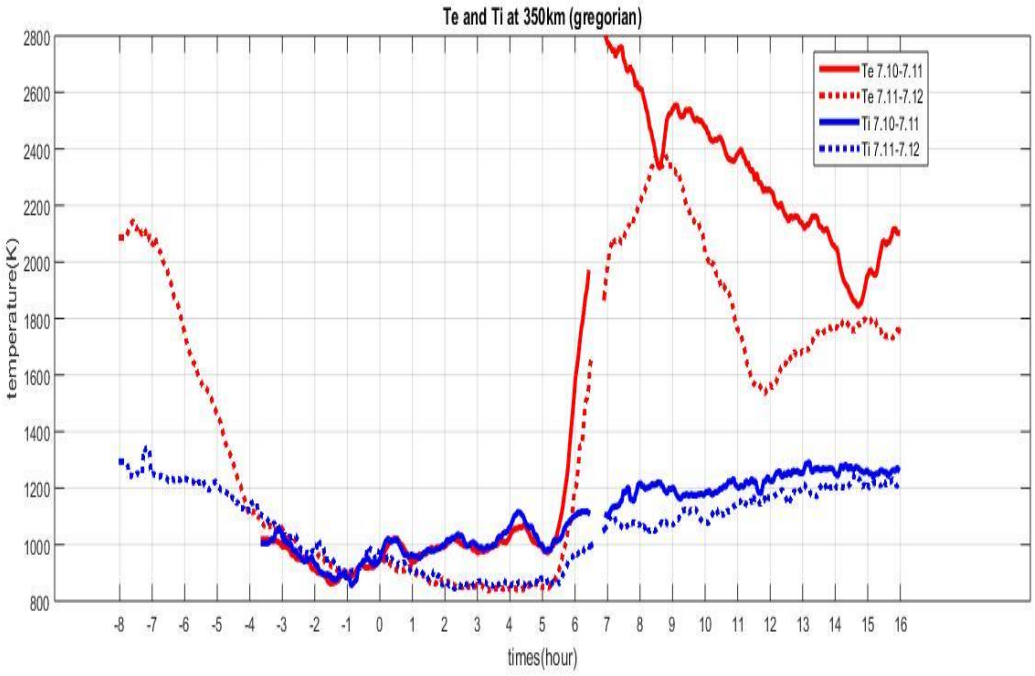

Figure 4.2 Variations of Te and Ti at 350km of two periods

Solid lines in Figure 4.2 represent the period during July 10 to July 11 and dash lines represent the period during July 11 to July 12. Red curves represent variation of Te at 350 km of two periods and blue curves represent Ti at 350 km of those periods. As the sun rises, red lines increase sharply and the red solid line increases to a higher temperature level (2800K) than the red dash line, which increases to about 2500K. One possible reason is that Ne from period July 10 to July 11 is larger than that of period July 11 to July 12. The Ti curves also show increment during sunrise hours, however, the increment is much less than that of Te curves. Blue solid line is higher than blue dash line during nighttime. They both increased to the same temperature level (100K) after sunrise.

4.2 Te/Ti ratio analysis

Electron to ion temperature (Te/Ti) ratio is an important indicator of the change between electron and ion temperature. It can help us to understand the potential processes of the ionosphere. Figure 4.3 (a) shows variation of Te/Ti ratio during 20:00 LT on July 10 to 17:00 LT on July 11 and Figure 4.3 (b) shows the variation of Te/Ti ratio during 17:00 LT on July 11 to 17:00 LT on July 12.

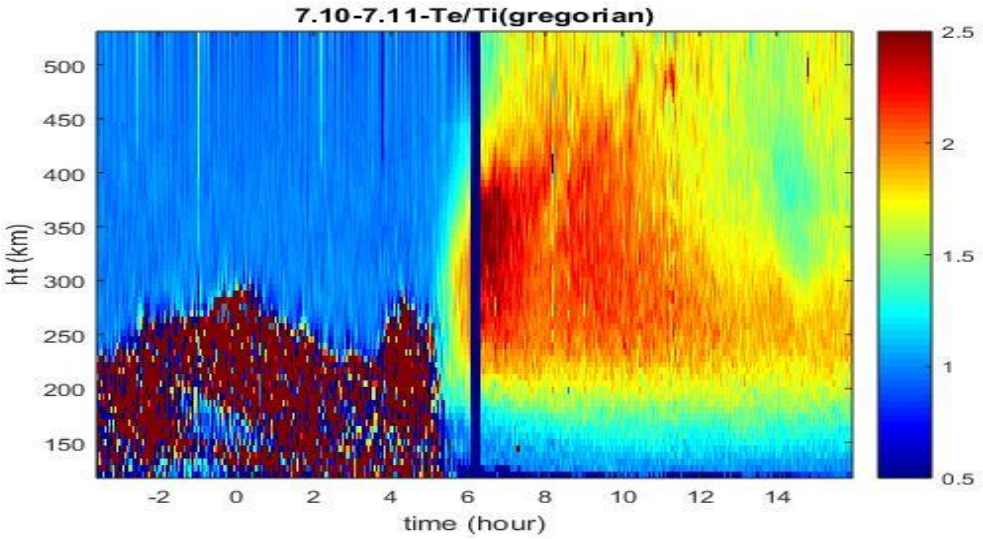

Figure 4.3(a) Variation of Te/Ti ratio during July 10 to July 11

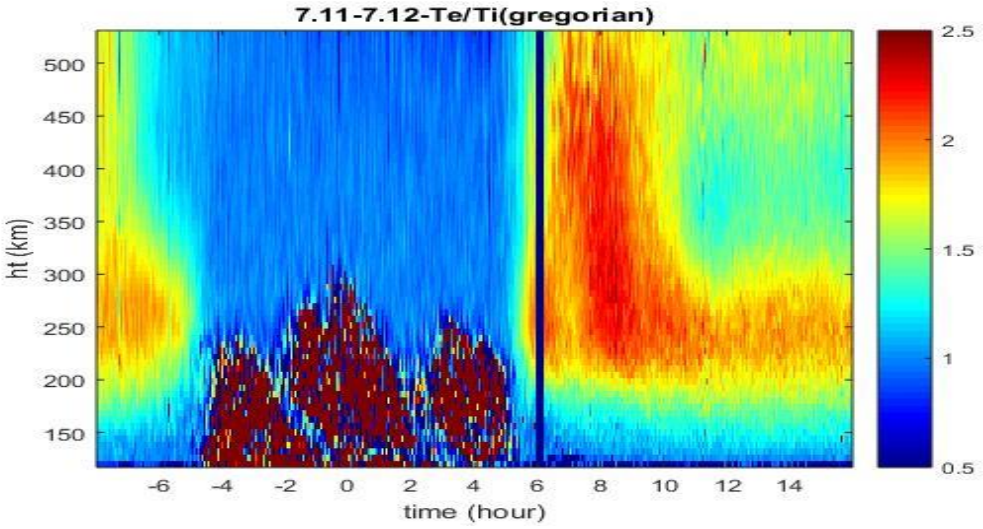

Figure 4.3(b) Variation of Te/Ti ratio during July 11 to July 12

As shown in Figure 4.3 (a) and (b), the daytime Te/Ti, July 11 is mostly larger than that July 12, during the daytime. We plot Te/Ti ratio at 300 km for these two periods for quantitative comparison in Figure 4.4.

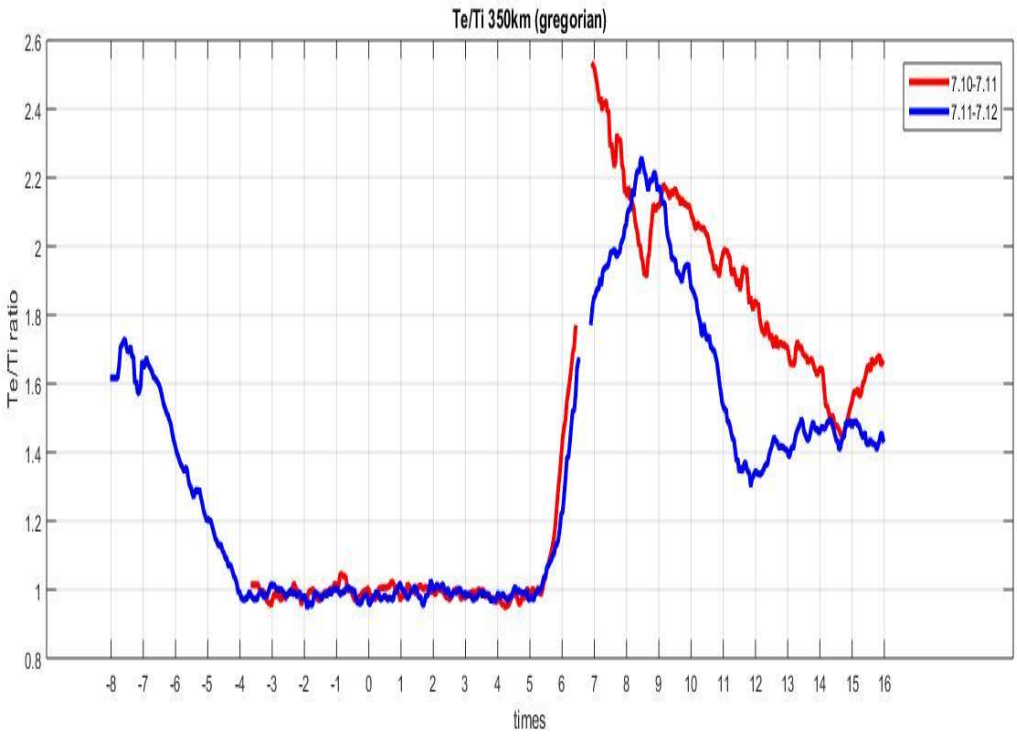

Figure 4.4 Variations of Te /Ti ratio at 350km of two periods

Red line represents Te/Ti ratio during July 10 to July 11 and blue line represents Te/Ti ratio during July 11 to July 12. From Figure 4.4, we can see Te/Ti ratio approximately equals to 1 during nighttime (20:00 LT-6:00 LT). That means electron and ion of 350 km had the same temperature during nighttime. During the sunrise hours, both curves increase sharply, but Te/Ti on July 11 increase much more than that of July 12. One interesting thing to note, however, is that there is a sharp drop in Te/Ti during the occurrence of F3 layer on July 11. Despite that Te/Ti is generally larger on July 11 than on July 12 during the daytime, it is smaller during the occurrence of the F_3 layer. Although we do not have a complete understanding of the F_3 layer occurrence at Arecibo, it is clear that its formation is strongly associated with horizontal inhomogeneity and temperature change.

Chapter 5 Conclusions and Future Work

This thesis presents studies on three aspects of ionospheric physics. The first aspect is an investigation of a rare F_3 layer phenomenon observed by Arecibo ISR on July 11, 2015. Second one is to study the ionospheric horizontal gradients at nighttime. Third one is a general study of derivation of vector velocity and an analysis of electron and ion temperatures.

Although the study of F_3 layer can be traced back to the middle of the last century and numerous studies on F_3 layer have been published, only a few of them focus on the Arecibo latitude and this thesis is the first time to report the F_3 layer phenomenon observed by the Arecibo ISR. Unlike the F_3 layers reported by other authors, this F_3 layer is not caused by the upward **ExB** drift. By means of EDP and Ne difference analysis, we get the conclusion that the F_3 layer, observed by the Gregorian feed, is mainly due to the horizonal inhomogeneity. Because of the small horizontal scale (~100 km) of the inhomogeneity, the source mechanism is likely gravity waves. It is also likely that there also exists some vertical inhomogeneity as well. For future, we can focus on the vertical gradient and build a 3-D gradient model for during the occurrence of the F_3 layer.

For nighttime horizontal gradient we analyzed the Ne difference and hmf2 difference. Through comparison and analysis at different time, day, altitude and radar feed, we can describe the variation of the horizontal gradient as a function of azimuth angle at different altitudes and analyze the general direction of the horizontal gradient. The data appear to show that variations and movement of ionosphere is caused by superposition of several waves. Large-scale motion and changes of ionosphere are likely related to tides and small-scale variations are related to gravity waves. For future work, we can study these waves and try to understand the mechanism for the horizontal gradient.

In Chapter 4, we have analyzed the differences and relationships between the Te,Ti and Te/Ti ratio with and without the F_3 layer. We find that the electron temperature before and after the occurrence of the F_3 was elevated. The ion temperature was elevated before, during and after

the occurrence of the F_3 layer. As a result, the ratio of electron to ion temperature was reduced when F_3 layer was observed.

BIBILIOGRAPHY

Balan, N., G. J. Bailey, M. A. Abdu, K. I. Oyama, P. G. Richards, J. Macdougall, and I. S. Batista (1997), Equatorial plasma fountain and its effects over three locations: Evidence for an additional layer, the F3 layer, J. Geophys. Res., 102, 2047.

Balan, N., I. S. Batista, M. A. Abdu, J. Macdougall, and G. J. Bailey (1998), Physical mechanism and statistics of occurrence of an additional layer in the equatorial ionosphere, J. Geophys. Res., 103, 29,169–29,181.

Balan, N., S. V. Thampi, K. Lynn, Y. Otsuka, H. Alleyne, S. Watanabe, M. A. Adbu, and B. G. Fejer (2008), F3 layer during penetration electric field, J. Geophys. Res., Vol. 113, A00A07, doi: 10/1029/2008jA013206, 2008

Bardhan, A., D. K. sharma, M.S. Khurana, M. Aggarwal, S. Kumar (2015), Electron-ion-neutral temperes and their ratio comparisons over low latitude ionosphere, Advances in Space Research 56 (2015) 2117-2129.

Beynon, W. J. G., Williams, P. J. S. (1978), Incoherent scatter of radio waves form ionosphere. Rep. Prog Phys.,41:6.

Bowles, K. L. (1958), Observations of vertical incidence scatter from the ionosphere at 41 Mc/s, Phys. Rev. Letters, 1, 454.

Buonsanto, M. J., and O. G. Witasse (1999), An updated climatology of thermospheric neutral winds and F region ion drifts above Millstone Hill, J. Geophys. Res., 104, 24,675– 24,687.

Elias, B., (2016), China completes world's largest radio telescope-raising hopes of finding new worlds and alien life. The Conversation. Academic rigor, journalistic flair.

Evans, J.V. (1969), Theory and practice of ionosphere study by Thomson Scatter Radar. THE IEEE INC, 57:496–530.

Gong, Y. (2012), Incoherent scatter study of dynamics in the ionosphere E-and F-region at Arecibo. A Thesis Submitted to the Faculty of Miami University.

Gordon, W. E. (1958), Incoherent scattering of radio waves by free electrons with applications to space exploration by radar, Proc. IRE, 46, 1824.
Hagfors, T., and R. A. Behnke (1974), Measurements of three-dimensional plasma velocities at the Arecibo Observatory, *Radio Sci.*, 9, 89– 93.

Heelis, R. A., P. C. Kendall, R. J. Moffet, D. W. Windie, and H. Rishbeth (1974), Electric coupling of the E and F regions and its effect on F region drifts and winds, Planet. Space Sci., 22, 743–756.

Kelly, M., The Earth's Ionosphere, 1st Edition Plasma Physics and Electrodynamics. ISBN: 9780323148054. Preface:xi.

Limberger, M., Pajares, M. H., Angel, A. A., Altadil., D. (2015), Long-term comparison of the ionospheric F2 layer electron density peak derived from ionosonde data and Formosat-3/Cosmic. J. Space Weather Space Clim., DOI: 10.1051/sesc/2015023

Mathews, J. D., A short history of geophysical radar at Arecibo Observatory, Hist. Geo Space Sci., 4,19-33, 2013

Nagarajoo, K. (2012), Variable methods to estiate the ionospheric horizontal gradient. IOP Conf.Series: Earth and Environmental Science 37 (2016) 012012

Nan, R. D. (2005), Five hundred meter aperture spherical radio telescope. Science in China: series G, 2006, Vol. 49, No. 2, 129-148.

Williams II, R. L., "Five-Hundred Meter Aperture Spherical Radio Telescope (FAST) Cable-Suspended Robot Model and Comparison with the Arecibo Observatory", Internet Publication, www.ohio.edu/people/williar4/html/pdf/FAST.pdf, July 2015.

Schunk, R.W., Nagy, A.F., 1978. Electron temperatures in the F region of the ionosphere: theory and observations. Rev. Geophys. Space Phys. 16, 355–399.

Sen, H. Y., (1949), Stratification of the F2-layer of the ionosphere over Singapore. Journal of Geophysical. Volume:54, Issue 4, Pages: 363-366.

Sulzer, M. P,. Mathews, J. D., and Tomko, A. A: A UHF cross-modulation D region heating experiment with aeronomic implications, Radio Science, 17, 435-443

Wang C. P., Gkioulidou, L. R. Lyons and V. Angelopoulos (2012), Spatial distributions of ion to electron temperature ratio in the magnetosheath and plasma sheet, J. Geophys, Res. Vol. 117, A08215, doi: 10.1029/2012JA017658

Williams, R. L. II (2015). Five Hundred Meter Aperture Spherical Radio Telescope Cable-Suspended Robot Model and Comparison with the Arecibo Observatory. Ohio University.

Zhao, B., W. Wan, X. Yue, L. Liu, Z. Ren, M. He, and J. Liu (2011), Global characteristics of occurrence of an additional layer in the ionosphere observed by COSMIC/FORMOSAT-3, Geophys. Res. Lett., 38, L02101, doi:10.1029/2010GL045744.

Zhou, Q. H., M. P. Sulzer, and C. A. Tepley (1997), An analysis of tidalan d planetary w aves in the neutr al winds and temperature observed atlow-la titude E region heights, J. Geop hys. Res., 102 , 11,491 11,505,doi:10.1029/97JA00440.

Zhou, Q. H., M. P. Sulzer, C. A. Tepley, C. G. Fesen, R. G. Robie, and M. C. Kelley (1997b), Neutral winds and temperature in the tropical mesosphere and lower thermosphere during January 1993: Observation and comparison with TIME-GCM results, J. Geophys. Res., 102, 11,507-11,519.